LIÈGE université Library

https://lib.uliege.be

https://matheo.uliege.be

Research master thesis

Auteur : Chilakalapudi, Prabhath
Promoteur(s) : Verstraete, Matthieu
Faculté : Faculté des Sciences
Diplôme : Master en sciences physiques, à finalité approfondie
Année académique : 2022-2023
URI/URL : http://hdl.handle.net/2268.2/18537

Avertissement à l'attention des usagers :

Tous les documents placés en accès ouvert sur le site le site MatheO sont protégés par le droit d'auteur. Conformément aux principes énoncés par la "Budapest Open Access Initiative"(BOAI, 2002), l'utilisateur du site peut lire, télécharger, copier, transmettre, imprimer, chercher ou faire un lien vers le texte intégral de ces documents, les disséquer pour les indexer, s'en servir de données pour un logiciel, ou s'en servir à toute autre fin légale (ou prévue par la réglementation relative au droit d'auteur). Toute utilisation du document à des fins commerciales est strictement interdite.

Par ailleurs, l'utilisateur s'engage à respecter les droits moraux de l'auteur, principalement le droit à l'intégrité de l'oeuvre et le droit de paternité et ce dans toute utilisation que l'utilisateur entreprend. Ainsi, à titre d'exemple, lorsqu'il reproduira un document par extrait ou dans son intégralité, l'utilisateur citera de manière complète les sources telles que mentionnées ci-dessus. Toute utilisation non explicitement autorisée ci-avant (telle que par exemple, la modification du document ou son résumé) nécessite l'autorisation préalable et expresse des auteurs ou de leurs ayants droit.

University of Liège

Faculty of Applied Sciences

Using Machine Learning Interatomic Potentials to Investigate Charge Density Waves in Monolayer Transition Metal Dichalcogenides

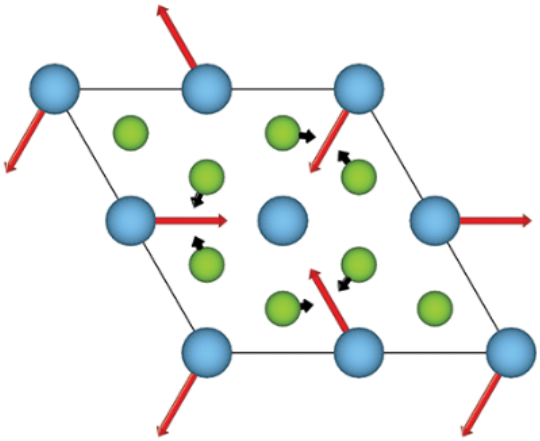

Master's thesis completed in order to obtain the degree of
Master of Science in Physics (*M2, FAME+*)

by - Prabhath Chilakalapudi.
Supervisor: Dr. Prof. Matthieu Verstraete
Advisor: Dr. Aloïs Castellano

Academic year 2022-2023

Abstract

Charge Density Waves (CDWs) are characterized by an instability of the electronic structure, that is coupled with a distortion in the atomic arrangement in a metal, leading to a decrease in energy (lower than the high symmetry phase) along with the appearance of an unstable phonon mode. CDWs in Transition Metal Dichalcogenides (TMDs) have been researched for the past four decades. Aided by the advancement of computational power and the development of computational methods, there have been successful attempts at simulating these CDWs using first principle methods [1, 2]. Although these methods are quite accurate, they are computationally very expensive, and hence there is a need for faster alternatives like classical Molecular Dynamics (MD) simulations. As a solution, we propose the use of Machine Learning Interatomic Potentials (MLIPs), fit to first principles calculations, in order to reduce simulation times and costs, while achieving near *ab initio* accuracy.

In this study, we compared two types of MLIPs - Spectral Neighbor Analysis Potential (SNAP) and Moment Tensor Potential (MTP), trained on a set of Density Functional Theory (DFT) that are *ab initio* calculations. They were then tested to investigate if they can reproduce the CDW distortion in two monolayer TMDs - 1T-$TiSe_2$ and 1T-TiS_2. The Python package 'MLACS' [3] is used for the ML training. The results of this thesis show that the chosen MLIPs are orders of magnitude faster than *ab initio* calculations, but might not be accurate enough. Phonons calculated using finite-difference approximation clearly show an unstable mode at the M point for monolayer 1T-TiS_2, indicating the CDW state as found in the literature [4]. Yet, no instability was found for the monolayer 1T-$TiSe_2$. The phonon modes were then calculated at finite temperatures using a theory of anharmonic vibrations called the Temperature Dependent Effective Potential (TDEP) [5]. TDEP is a method to calculate the free energy of a system and not

just the potential energy. It renormalizes all orders of anharmonicity as well and makes it perfect for our research. Phonons calculated using TDEP do not show an instability, which could be a limitation caused by the potential's accuracy or even the DFT "ground truth" calculations. This study hence demonstrates that MLIPs calculated can be used for MD simulations, but have certain limitations.

Acknowledgement

The successful completion of my Master's dissertation has been made possible by many benefactors. I extend my sincere appreciation to each of them for their contributions to my research journey.

Foremost, I express my gratitude to Dr. Prof. Matthieu Verstraete, the Principal Investigator, for providing me with the opportunity to engage in this enriching research endeavour. His guidance, mentorship, and unwavering encouragement throughout has been invaluable to me. I am indebted to Dr. Aloïs Castellano for supervising my research project, providing constructive feedback, and offering assistance during challenging times, which significantly aided my progress. I acknowledge with gratitude the insights and collaborative spirit of Jose Pedro Batista, which played an integral role in the completion of this project. Dr. Bogdan Guster's comprehensive theoretical teachings enhanced my proficiency in subject. Max Mignolet's invaluable assistance with coding obstacles proved instrumental in navigating the research process. I am appreciative of Samuel Longo's engaging discussions and idea exchanges, which enriched our research group's intellectual environment. Louis Bastogne's patient instruction in Density Functional Theory (DFT) expanded my knowledge and skills appreciably.

My heartfelt appreciation extends to the computing clusters pivotal to my research's computational aspects: The CÉCI clusters, including NIC5, Zenobe, and Lucia, provided vital computing resources for simulations and analysis. The Discoverer cluster, (a Bulgarian computing resource), facilitated various research facets.

The biggest pillars of support have been my family and friends. I am overwhelmed with gratitude towards my parents Vasantha and Dasaratha Ram for their unfailing belief in my capabilities. I am very grateful to my brother Praneeth and sister-in-law Sunayana for never having left my side. I would like to

thank my friends Anasua, Gaurav and Shourjo for their company and support when I needed it.

Contents

List of Figures

List of Tables

Nomenclature

$AIMD$	*ab initio* Molecular Dynamics
ASE	Atomic Simulation Environment
CDW	Charge Density Waves
$DFPT$	Density Functional Perturbation Theory
DFT	Density Functional Theory
FD	Finite Difference
FSN	Fermi Surface Nesting
GAP	Gaussian Approximation Potential
GGA	Generalized Gradient Approximation
IFC	Interatomic Force Constant
LDA	Local Density Approximation
mBJ	modified Becke-Johnson
MD	Molecular Dynamics
$MLACS$	Machine Learning Assisted Canonical Sampling
$MLIP$	Machine Learning Interatomic Potentials

$MLMD$ Machine Learning Molecular Dynamics

MTP Moment Tensor Potential

NNP Neural Network Potential

PBE Perdew–Burke-Ernzerhof

PES Potential Energy Surface

PLD Periodic Lattice Distortion

$RMSE$ Root Mean Square Error

$SCAN$ Strongly Constrained and Appropriately Normed

SCF Self Consistent Field

$SNAP$ Spectral Neighbour Analysis Potential

$TDEP$ Temperature Dependent Effective Potential

TMD Transition Metal Dichalcogenides

1 Introduction

Charge Density Waves (hereby referred to as CDWs) have been an alluring topic of research [1, 2, 4] for many decades now. They appear because of an electronic instability that translates into a Periodic Lattice Distortion (PLD). They have been researched upon because of their influence on electrical properties and their relation with superconductivity in materials [6]. There have been multiple computational studies on different materials containing CDWs using *ab initio* methods, but not using classical potentials.

To understand the behavior of a material, knowledge of its interatomic potential energy plays a very important role. Minimizing this potential energy will give the ground state structure of the system. This potential energy of the system can be found, for example - by using *ab initio* methods such as Density Functional Theory (DFT) and other electronic structure methods, or using classical potentials. Once the interatomic potential energy has been found, the next step is to study the lattice dynamics to understand the interplay between the electrons and phonons, in order to extract physical properties such as thermal conductivity, phase transitions etc. Properties also change with temperature and hence we need methods to find temperature-dependent equilibrium structures and the system's evolution with temperature.

Accurate methods such as *ab initio* Molecular Dynamics (AIMD) are very computationally intensive and require a lot of time. But, in order to save time, one cannot use only classical molecular dynamics because of its lower accuracy. As a solution and as a compromise between the accuracy and speed of calculation, this study proposes the use of Machine Learning Interatomic Potentials (referred to as MLIPs from here onwards). This study aims to be a proof of concept depicting advancement in MLIPs, leading them to be able to accurately predict quantum phenomena such as CDWs.

This chapter gives an overview of what CDWs are and their origin, what MLIPs

are, and other essential topics whose knowledge is required to understand this thesis.

1.1 Charge Density Waves (CDWs)

1.1.1 What are CDWs?

Crystalline metals are characterized by their uniform electron density and their perfectly periodic lattices in their equilibrium state. However, in certain cases, below a transition temperature (T_{CDW}), the electron density gets reordered into a standing wave with a periodic increase and decrease in electron density (peaks and troughs), instead of being fully uniform. This change leads to a reordering of the perfectly periodic lattice into new equilibrium positions by distorting the atomic positions with a longer periodicity. The resulting low-temperature state, where there is a modulation of the electronic density is hence called the Charge Density Wave (CDW) state.

Origins of CDWs

CDWs are quite system dependent. There are multiple explanations for why they occur, such as Peierls' instability, electron-phonon coupling, and Fermi surface nesting. However, there is none that can uniformly explain the origin of CDWs in all materials. The two distortions - lattice and electronic density, do not occur together by coincidence. The CDW formation relies on the lattice distortion, meaning that a strong electron-phonon coupling is necessary to drive it. But, there is a debate on whether the instability observed is primarily that of the lattice or the electronic system.

The most widely accepted model is that of the *Peierls' instability* in 1D. This model is an explanation of how the ionic/lattice distortion is a secondary effect that occurs due to the electronically driven charge redistribution. Figure 1.1 from Ref.[7] gives a schematic representation of the Peierls description of instability for a 1D case. Figure 1.1(a) shows a 1D chain with a periodic lattice (above the transition temperature T_{CDW}), while Figure 1.1(b) shows the restructured lattice with the Periodic Lattice Distortion (PLD).

Figure 1.1(c) shows the electron band structure (in reciprocal space) for the 1D undistorted chain, around the Fermi level. The material is in a metallic state and hence there is no bandgap. The Brillouin zone boundary is located at $\pm\frac{\pi}{a}$ (where a is the cell parameter), while the Fermi wave vector (k_F), that defines the highest energy electron, is at $k_F = \pm\frac{\pi}{2a}$. This structure is unstable at lower temperatures and causes the lattice to get disturbed. Figure 1.1(b) shows the distortion as a dimerization. This means two adjacent lattices have combined to

form a new unitcell. The new cell parameter is $2a$ and the Brillouin zone reduces to half its original size, to $\pm\frac{\pi}{2a}$. The coincidence of the k_F with the new Brillouin zone boundary opens up a band gap, creating the transition of the material from a metal to a semiconductor. This distortion is hence associated with an increase in the energy of the system. The electronic instability that causes this transition was given the name *Peierls' instability*.

Such instabilities in materials can be understood using the knowledge of phonons (as will be described in Section 2.3.1) and their soft modes. The above-mentioned transition can be measured by studying temperature-dependent phonons. The transition to the semiconductor phase occurs because of a highly unstable phonon mode present in the metallic phase. This is termed as the *Kohn anomaly*.

An additional reason behind the creation of the CDW can be attributed to a phenomenon known as Fermi Surface Nesting (FSN). The Fermi surface denotes the boundary that separates the occupied and unoccupied electron states. Within the reciprocal lattice, it outlines a collection of momentum points where electrons possess their maximum energy at absolute zero temperature. Nesting is a process where specific sections of a material's Fermi surface exhibit highly resembling shapes and begin to closely align within the momentum space. Put differently, there exists a significant overlap between the momentum vectors linking equivalent points on both Fermi surfaces. The occurrence of Fermi surface nesting directs the potential toward a more energy-efficient arrangement in the system. This lowered energy state can be attained by allowing electrons to transition between the nested regions, thereby minimizing the overall electronic energy. Consequently, the material's crystal lattice undergoes a spontaneous distortion to accommodate this more energy-efficient arrangement.

1.1.2 CDWs in Transition Metal Dichalcogenides (TMDs)

Transition metal dichalcogenides (TMDs) are a class of materials that consist of layers of transition metal atoms sandwiched between two layers of chalcogen atoms. Their general chemical formula is MX_2, where M represents a transition metal element and X represents a chalcogen element. TMDs have been experimented upon for a very long time now. Amongst them, the existence of CDW in the compounds 1T-$TiSe_2$ and 1T-TiS_2 (where "1T" is the tetragonal phase with a $P\bar{3}m1$) has been a matter of debate for both experimentalists and theoreticians. A deep look into the literature available shows us the need for a more extensive study on these compounds. Figure 1.2 is a schematic of the layered structure of 1T-$TiSe_2$ from Ref. [1]. Figure 1.2(c) shows the direction of displacements of each atom while the material transitions from the high symmetry phase to the periodically distorted CDW phase.

Currently, the literature reports a difference between what is found in experi-

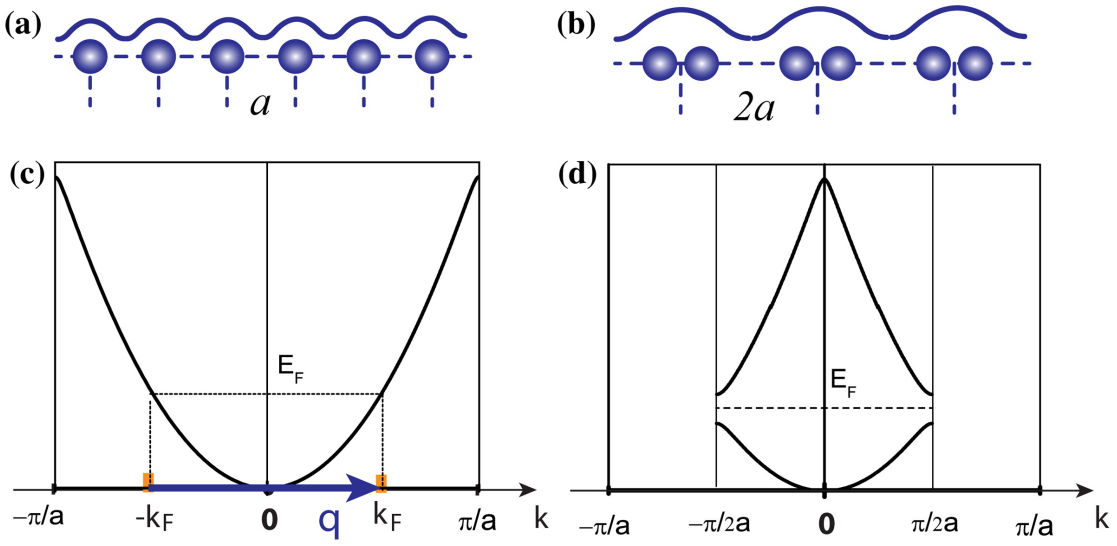

Figure 1.1: Schematics of the Charge Density Waves from Ref.[7] showing (a) 1D atomic chain with uniform electron density (above transition temperature T_{CDW}), (b) 1D atomic chain with restructured atom sites and electron density (below T_{CDW}), (c) electron band structure of the metal phase above T_{CDW} and of (d) the semiconductor phase below T_{CDW}

ments and simulations. For example, the experimentally found T_{CDW} in monolayer 1T-$TiSe_2$ is 200K [8], while DFT (*ab initio*) studies show a T_{CDW} of 440K. As for 1T-TiS_2, experimental studies of the electronic structure give qualitatively different results for the bandgap - some say it is a semiconductor [9], while others find a semimetal [10]. Such a difference in the experimental results might be due to the different growth conditions used. On the other hand, DFT studies of 1T-TiS_2 show a dependence of the CDW state on dimensionality - beneath a thickness of 4 monolayers [4]. An accurate potential that can be used for classical Molecular Dynamics (MD) will hence aid this direction of research strongly and motivated this Master's thesis project.

Figure 1.3(a) is a plot showing the temperature dependence of the phonons for monolayer 1T-$TiSe_2$, from Ref [1], calculated using DFT. Figure 1.3(b) from Ref.[2] shows a schematic of the Brillouin zone of a 1T lattice. It clearly shows the strong instability at the M point (with the reciprocal space vector $\left[\frac{\pi}{a}, -\frac{\pi}{\sqrt{3}a}, 0\right]$), and how the instability reduces with increasing temperature. There are similar reports for the M point instability for monolayer 1T-TiS_2 as well [4]. The motivation behind this study is to try to reproduce this very instability in both materials using MLIPs that are fit on accurate *ab initio* data.

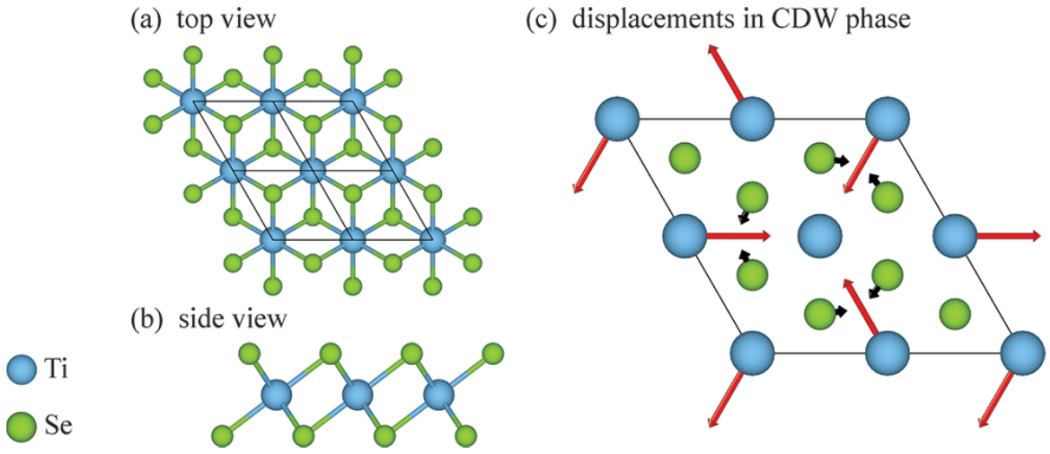

Figure 1.2: Schematic of the lattice structure of monolayer 1T-$TiSe_2$ from Ref.[1], and the atomic displacements associated with the Periodic Lattice Distortion associated with the CDW phase transition

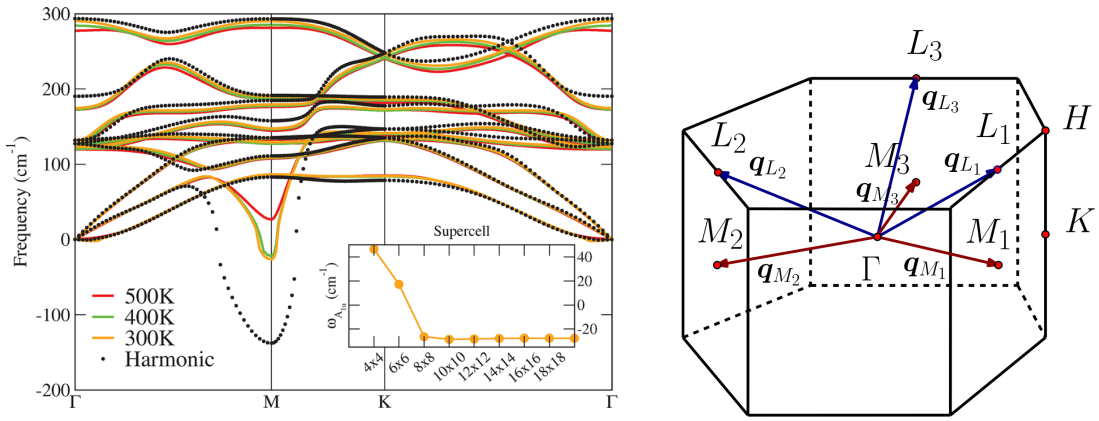

(a) (b)

Figure 1.3: (a) Temperature-dependent phonon dispersion curve from Ref.[1] for monolayer 1T-$TiSe_2$; (b) Schematic of the Brillouin zone from Ref.[2] of octahedral TMDs (like 1T-$TiSe_2$)

1.2 Why Machine Learning Interatomic Potentials (MLIPs)?

Theoretical research must always deal with tradeoffs between methods that give very quick and inaccurate results or slow but accurate results. MLIPs are a

set of numerical and non-empirical potentials that offer the best of both worlds. Amongst all the available methods of calculating interatomic potentials, empirical or otherwise, the usage of MLIPs seems to be an extremely promising prospect. They are trained on *ab initio* data but are then used to calculate system properties using fast classical methods. Once trained on a given limited set of *ab initio* data, these MLIPs can run simulations with near *ab initio* accuracy, but thousands of times faster. Machine learning and MLIPs have hence been used in simulations for about a decade now, in a very wide variety of domains [11, 12, 13, 14].

There have been advancements in the MLIPs themselves, as new and improved methods have been developed. The most popular and efficient are - Gaussian Approximation Potentials (GAP), Neural Network Potentials (NNP), the Spectral Neighbour Analysis Potential (SNAP), and the Moment Tensor Potential (MTP).

This thesis is a study of how two of the above-mentioned MLIPs - SNAP and MTP perform with regard to learning delicate temperature-dependent mechanisms such as CDWs and how MLIPs can help accelerate their study. These methods have been chosen for their greater efficiency. Unlike methods like NNP, these do not require a large volume of data to fit the MLIP. They are also quick to train and are faster to execute as compared to GAP.

2 Methodology

This chapter elaborates in detail the methods and tools we used to study CDWs in the chosen monolayer TMD materials 1T-$TiSe_2$ and 1T-TiS_2.

2.1 *ab initio* calculations

As explained in the abstract, the goal of this study involves training an MLIP on a given dataset. The dataset is made of different configurations of the given system whose energies, forces, and stress are calculated with *ab initio* accuracy. This section explains how these configurations are created.

2.1.1 Density Functional Theory (DFT) - an *ab initio* method

The current state of the art in electronic structure simulations are *ab initio* methods, which give accurate results with a cost scaling as the cube of the number of electrons (or more for higher order methods). In order to create the configurations mentioned above and calculate their ground state energies, we will use Density Functional Theory (DFT [15]). DFT is a method where the energy of a many-electron system is determined by using its electronic density instead of the full many-body wave function. In this study, we use the software Abinit [16], for all the calculations involving DFT.

The Hohenberg-Kohn theorems [15] provide the theoretical foundation for density functional theory, stating that the electron density uniquely determines the ground-state energy and vice versa. However, in practice, solving the many-body Schrödinger equation for a many-electron system is computationally challenging due to the complexity of electron-electron interactions.

A practical solution was given to this problem in the form of the Kohn-Sham

equation (Equation (2.1)) [17]. This theory considers fictitious orbitals (called the Kohn-Sham orbitals) that are designed to have the same electron density as the real system.

$$\left[-\frac{\hbar^2}{2m}\nabla^2 + \underbrace{V_{\text{ext}}(\mathbf{r}) + V_{\text{xc}}(n(\mathbf{r})) + \int \overbrace{\frac{n(\mathbf{r}')}{|\mathbf{r}-\mathbf{r}'|}}^{V_H} d\mathbf{r}'}_{V_{\text{eff}}}\right]\psi_i(\mathbf{r}) = \epsilon_i\psi_i(\mathbf{r}) \tag{2.1}$$

where $-\frac{\hbar^2}{2m}\nabla^2$ is the kinetic energy, $n(\mathbf{r})$ is the net electron density (defined below) $V_{\text{ext}}(\mathbf{r})$ is the external potential on the system which includes the interaction of electrons with external fields (for example, atomic nuclei), $V_{\text{H}}(\mathbf{r})$ is the Hartree potential which represents the electrostatic repulsion between electrons, and $V_{\text{xc}}(\mathbf{r})$ is the exchange-correlation potential that accounts for the quantum mechanical effects of electron exchange and correlation.

The net electron density ($n(\mathbf{r})$) proposed by Kohn and Sham [17] is given in equation Equation (2.2) , where ψ_i is the wave function of each Kohn-Sham orbital of the system. The DFT implementation used in this study (using the software Abinit) uses a plane wave basis set for these wave functions.

$$n(\mathbf{r}) = \sum_{i=1}^{N} \mid \psi_i(\mathbf{r}) \mid^2 \tag{2.2}$$

The wavefunction $\psi_i(\mathbf{r})$ (the eigenvalues of the above equation) and energy ϵ_i are the solutions to the Kohn-Sham equation for the i^{th} electron. In our case, for the V_{xc}, we use the Generalized Gradient Approximation (GGA), which incorporates the gradient of the electron density as well.

The Hamiltonian, given by the Kohn-Sham equation (Equation (2.1)) governs the DFT calculation in the form of a self-consistent field. The density is calculated in a loop and is iteratively optimized (known as Self Consistent Field (SCF)) to within a given tolerance for which the eigenstates which solve the equation also produce the input density.

The DFT implementation in Abinit uses what is called a pseudopotential. It replaces the V_{H} and V_{xc} due to core electrons and the V_{ext} due to the nucleus with an effective potential. This is done to make sure that the Schrödinger equation does not take into account the Coulombic potential term for core electrons.

2.1.2 Convergence of the DFT parameters for the unitcell

There are many variables such as the choice of basis set, and k-point grids that go into calculating the ground state energy of a system using DFT. The basis set defines the Kohn-Sham orbitals used by DFT ($\psi_i(\mathbf{r})$). k-points are sampling

points in the first Brillouin zone of a material. The Brillouin zone is defined better with an increase in the density of the k-point grid. These variables need to be optimized in order to get an accurate enough result in the minimal possible time. Hence, there is a need to perform a convergence study on these parameters and determine their optimal values.

The structures of monolayer 1T-$TiSe_2$ and 1T-TiS_2 have been known for a very long time and hence can easily be found on websites like the Materials Project [18]. But, in order to calculate the ground state energy using DFT, for the specific exchange-correlation functional that is being used (PBE-GGA [19]), the calculation precision needs to be converged with respect to each of the variables discussed below.

- **Kinetic energy cut off for the pseudopotential** - The number of plane waves that are needed to integrate accurately the total energy, mainly imposed by the pseudopotential.

- **Size of the *k*-point grid chosen** - The density/number of points on the Brillouin zone that the wave functions will be evaluated at.

- **Electronic temperature** - The variable to ensure physically correct occupation of electronic bands around the Fermi level. It also depends on the statistical model (such as Gaussian or Fermi-Dirac statistics)followed to "smear" these electrons.

- **Interlayer distance** - Since DFT assumes a periodic boundary, the interlayer distance for a non-monolayer system can be increased to a point where there is very little interlayer interaction.

- **Cell parameters/ relaxation** - Minimization of the pressure in the system, hence relaxing it to its ground state.

Once all the parameters are converged for the unit cell, supercells can be constructed from it.

2.2 Classical Molecular Dynamics (MD)

In stark contrast to the *ab initio* methods, classical Molecular Dynamics (MD) uses classical potentials (and not DFT) to govern the atoms along their potential energy surface (PES). This method is hence very quick in comparison to a method such as DFT. Yet MD offers much lower accuracy if empirical/semi-empirical potentials are used to calculate the PES.

In MD simulations, systems are considered to be a part of specific ensembles such as the canonical (NVT), grand-canonical (μVT), etc., that define the degrees of freedom that each atom possesses. In order to force such degrees of freedom to remain constant (such as constant temperature or pressure), specific barostats and thermostats are defined.

In the numerical implementation of MD, the Nose-Hoover thermo/barostat [20] and the Langevin thermo/barostat are the most commonly used methods. Both these methods make sure that the average kinetic energy of the system remains constant, following the equipartition theorem for the canonical ensemble. To simulate NPT, an additional barostat needs to be added to the system.

In the scope of this study, classical MD simulations are used to replace the tedious AIMD (*ab initio* Molecular Dynamics) simulations. Machine Learning has been used to create classical potentials that can do this job very well, hence closing the distance between AIMD and MD through MLMD (Machine Learning Molecular Dynamics). MD simulations have been used in this study extensively and will be explained in the next sections.

2.3 Calculation of phonon curves

2.3.1 What is a phonon?

A phonon is defined as a quantum of mechanical vibration for a given periodic lattice, representing a long-range collective oscillation in an elastic manner. Knowledge of the phonons of a lattice allows one to calculate material properties such as thermal conductivity [21]. Properties such as electrical conductivity can also be calculated by understanding phonons in combination with the electron-phonon coupling. In this study, for example, a change in phonon frequency at a specific point in the Brillouin zone describes the onset of a Charge Density Wave (CDW). There are multiple methods to calculate phonons and the most common ones are described in the following subsection.

Before advancing, it is important to understand what the Interatomic Force Constant (IFC) is. The IFC is usually derived using the harmonic approximation as given in the Equation (2.3) below. We perform a Taylor series approximation of the potential until the second-order term.

$$\mathrm{V}(R) \approx \mathrm{V}(R_0) + \cancelto{0}{\left.\frac{\partial V(R)}{\partial R}\right|_{R_0} u} + \frac{1}{2}\left.\frac{\partial^2 \mathrm{V}(R)}{\partial R^2}\right|_{R_0} u^2 \tag{2.3}$$

where $u = R - R_0$ is the displacement of atoms about their equilibrium position at R_0. The second term - the first derivative of the potential at R_0 is 0, as

it is a minima. Simplifying Equation (2.3), we get a double sum as given in Equation (2.4).

$$\mathrm{V}(R) \approx \mathrm{V}(\mathbf{u}) = \frac{1}{2}\sum_{l\kappa}\sum_{m\mu}\Phi_{l\kappa}^{m\mu}u_l^{\kappa}u_m^{\mu} \tag{2.4}$$

where $\Phi_{l\kappa}^{m\mu}$ is the IFC and κ and μ denote the unit cell index, and u_l^{κ} denotes the displacement around the equilibrium position.

The dynamical matrix is defined as:

$$\Phi_{l\kappa}^{m\mu} = \left.\frac{\partial^2 V(\mathbf{R})}{\partial R_l^{\kappa}\partial R_m^{\mu}}\right|_{R_0} \xrightarrow{Fourier\,Transform} D(\mathbf{q}) = \sum_{m\mu}\frac{\Phi_{l\kappa}^{m\mu}}{\sqrt{M_\kappa M_\mu}}e^{i\mathbf{q}\mathbf{R}_m} \tag{2.5}$$

where q, M_κ and M_μ are the masses of the interacting atoms. Diagonalizing this dynamical matrix $D(\mathbf{q})$ (making it an eigenvalue equation) and calculating the eigenvalues gives the phonon frequencies ω^2. ω^2 is hence the curvature of the potential energy surface at a given point. A phonon mode (of vibration) is said to be stable if the curvature is greater than 0, and unstable if it is negative (making ω imaginary). In specific cases such as CDWs as mentioned above, it has been found that there is a strong unstable phonon mode (large imaginary value of ω) associated with it. Knowledge of phonons hence helps us in determining if the given state of the system will transform into the CDW state.

The next sections describe how we can calculate the IFC (Φ) and further calculate the phonons themselves using different techniques.

2.3.2 Calculating phonons using Finite-Difference method

Calculating the phonon dispersion curve is quite straightforward when using the Finite-Difference method. It gives a broad idea of whether our potential is able to reproduce the same curves as with DFT. For this, the package *Phonopy* [22, 23] was used. It is important to mention that this method does not take into consideration temperature effects and hence gives the curve corresponding to the $T = 0K$ DFT data.

The calculation of phonons begins with the calculation of the Interatomic Force Constants (IFCs, Φ_{ij}), defined (same as in Equation (2.5)) as the second derivative of potential energy (Equation (2.6)). Φ is also the first derivative of the forces.

$$\mathbf{\Phi}_{ij} = \left.\frac{\partial^2 V(\mathbf{R})}{\partial \mathbf{R}_i \partial \mathbf{R}_j}\right|_{\mathbf{R}_0} = -\left.\frac{\partial f_i(\mathbf{R})}{\partial \mathbf{R}_j}\right|_{\mathbf{R}_0} \tag{2.6}$$

Using the finite difference approximation, the IFC (Φ_{ij}) can be calculated as follows. The forces can be obtained by either DFT calculations of different supercells, or from other methods such as using MLIPs.

$$\mathbf{\Phi}_{ij} = -\frac{\partial f_i(\mathbf{R})}{\partial \mathbf{R}_j}\bigg|_{\mathbf{R}_0} \approx -\frac{f_i(\mathbf{R}_0 + \delta\mathbf{R}_j) - f_i(\mathbf{R}_0)}{\delta\mathbf{R}_j} \tag{2.7}$$

where $\delta\mathbf{R}_j$ is a very small displacement of atom j, and $f_i(\mathbf{R}_0) \to 0$. The Fourier transform of these Φ_{ij} gives the phonon frequencies.

This method, however, has a few drawbacks - long-range interactions are not considered, it is very susceptible to noise from the DFT data, it has finite-size effects, and it requires the calculations to be performed on supercells.

A solution to these problems is the Density Functional Perturbation Theory (DFPT). DFPT is based on the concept of linear response theory, which deals with how a system's properties change in response to small perturbations. In the case of DFPT, the perturbations typically involve small atomic displacements from their equilibrium positions. Yet, our goal here is to be able to calculate phonon dispersion curves using the MLIPs we fit. The next section explains how this can be achieved.

2.3.3 Temperature Dependent Effective Potential (TDEP)

The finite difference method does not involve temperature-dependent calculations as the corresponding potential energy does not evolve with T. For our case of CDWs, we have a strong dependence on temperature and hence require a method to calculate phonons at specific temperatures. We have chosen to employ the Temperature Dependent Effective Potential (TDEP) [5, 24, 25, 26] method. TDEP calculates the free energy of the system and renormalizes all orders of anharmonicity.

We begin the formulation with the Hamiltonian, under the assumption that the system follows the canonical ensemble. The Hamiltonian is given as follows by Equation (2.8).

$$\mathrm{H} = \sum_i \frac{\mathbf{P}_i^2}{2M_i} + V(\mathbf{R}) \tag{2.8}$$

The next assumption is that the atoms vibrate around an equilibrium position $\langle\mathbf{R}\rangle$. The above Hamiltonian can hence be written as given below in Equation (2.9) and Equation (2.10). This is now the effective harmonic Hamiltonian.

$$\tilde{\mathrm{H}} = \sum_i \frac{\mathbf{P}_i^2}{2M_i} + \tilde{V}(\mathbf{R}) \tag{2.9}$$

$$\begin{aligned}\tilde{V}(\mathbf{R}) &= \frac{1}{2}\sum_{i,j}(\mathbf{R}_i - \mathcal{R}_i)\mathbf{\Theta_{i,j}}(\mathbf{R}_j - \mathcal{R}_j) \\ &= \frac{1}{2}\sum_{i,j}\mathbf{u_i}\mathbf{\Theta_{i,j}}\mathbf{u_j}\end{aligned} \tag{2.10}$$

where $\mathcal{R}_i$ are the effective equilibrium positions and $\mathbf{\Theta_{i,j}}$ are the effective (now temperature dependent) Interatomic Force Constants (IFCs). The free energy associated with the Hamiltonian is given by Equation (2.11).

$$\tilde{\mathcal{F}}_0 = -k_B T \ln[\tilde{\mathcal{Z}}] \tag{2.11}$$

where $\tilde{\mathcal{Z}}$ is the partition function of the effective harmonic potential at temperature T, given by -

$$\tilde{\mathcal{Z}} = \int d\mathbf{R} e^{-\beta\tilde{V}(\mathbf{R})} \tag{2.12}$$

To find the extremum of the Free energy ($\tilde{\mathcal{F}}_0$), we need to equate its gradient with respect to the IFCs to 0, the result of which is given in Equation (2.13)

$$\nabla_{\mathbf{\Theta}}\tilde{\mathcal{F}}_0 = \frac{\langle \mathbf{u}^{\mathrm{T}}\mathbf{u}\rangle_{\tilde{V}}}{2} \tag{2.13}$$

It can further be shown [27] that the effective IFC for the canonical ensemble is given by the following Equation (2.14).

$$\mathbf{\Theta} = \frac{k_B T}{\langle \mathbf{u}^{\mathrm{T}}\mathbf{u}\rangle} \tag{2.14}$$

TDEP, unlike the harmonic approximation, is not a calculation that is performed only in the locality of the equilibrium position of the atoms. Instead, the set of possible positions of the canonical ensemble is taken into consideration, and the anharmonic theory is applied to the average position and not the equilibrium position. Along with this, as mentioned above, it is the free energy that is calculated and not only the potential energy. This makes it very useful for temperature-dependent calculations. It renormalizes all orders of anharmonicity, hence giving more accurate results.

In order to run TDEP calculations, we need the average position of the atoms and their distribution in the canonical ensemble. Additionally, if we need to look at temperature dependence, we need to make sure that the material's thermal expansion is taken into consideration. We hence used a stepwise calculation procedure-

- **Step 1** - A supercell (whose size is a convergence parameter) is created from the unit cell of the high symmetry phase.

- **Step 2** - This supercell is allowed to evolve at the specific temperature according to the isobaric-isothermal ensemble (NPT) to allow room for thermal expansion for that temperature. The configurations created are averaged to get the reference unit cell size.
- **Step 3** - A new supercell is created using this unit cell and is now allowed to evolve according to the canonical ensemble (NVT). We now have the correct average cell and positions of the atoms from the first NPT run, and the correct distribution of the atomic positions for the NVT ensemble, which are required for TDEP.
- **Step 4** - TDEP calculations are then performed to calculate the phonon dispersion curves.

For all the above-mentioned calculations, in order to get *ab intio* accuracy, we need to use methods such as AIMD. As mentioned before, such methods are very computationally expensive and time-consuming. We hence adopted the Machine Learning route, as will be explained in further sections.

2.4 MLIPs

As explained in Section 1.2, MLIPs offer a very strong benefit - they do not oblige us to compromise between accuracy and speed of calculation. Unlike empirical and semi-empirical potentials that depend on some kind of experimental data, our MLIPs are purely numerical and are trained on highly accurate electronic structure numerical calculations. This section goes into detail on the chosen MLIPs, how they are constructed, and their advantages and disadvantages.

2.4.1 Structure of an MLIP

The end goal of an MLIP is to be able to define the potential, the energy, and the forces of a previously unseen configuration. As for this new configuration, all we have is the data of its structure, i.e., the atomic positions. MLIPs use different methods to translate these atomic positions into energy, forces, etc.

When an MLIP is learning from a given data set, it follows a sequence of steps to calculate and understand the atomic interactions. The atomic positions are first transformed into what is called a *descriptor*, a (usually nonlinear) function of the positions, which is rotationally and translationally invariant, and chosen to streamline the following steps (there are more properties of a descriptor that will not be discussed in this thesis). Once a list of *descriptors* is calculated, a Machine Learning (ML) model will be used (such as linear regression, neural network, or

other functional form) to learn a pattern from these different configurations. The pattern is then used to find the energy/potential of the new configuration. Figure 2.1 is a simple schematic that describes the same.

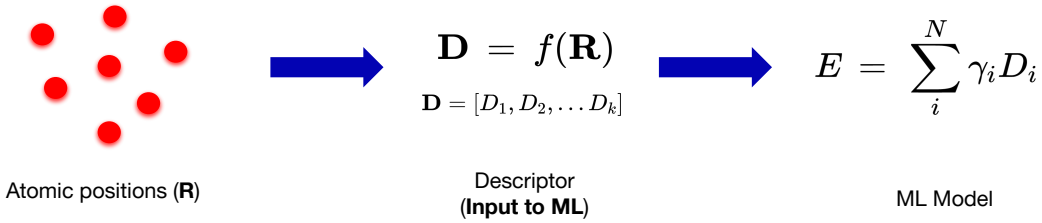

Figure 2.1: The stepwise sequence involved in creating an MLIP from a set of configurations for a simple linear fit

2.4.2 The chosen MLIPs

MLIPs have existed for a long time now and there have been extensively used, as mentioned in Section 1.2. Over the years, many ML methods such as Neural Networks (NN), Gaussian Approximation Potentials (GAP)[28], Moment Tensor Potentials (MTP)[29] and Spectral Neighbour Analysis Potential (SNAP)[30] have been developed to calculate interatomic potentials[31]. Figure 2.2 from Ref.[32] shows a plot of the performance assessment of some of the commonly used MLIPs found in the literature. Different metrics are chosen to determine which MLIP performs the best. Based on the properties being calculated, it can be based on the error in forces, energy, stresses, etc.

Two of the most efficient MLIPs - Spectral Neighbour Analysis Potential (SNAP) and Moment Tensor Potential (MTP) were chosen in order to make a comparison in their performance for CDW. The next subsections discuss in detail how these potentials are mathematically formulated.

Spectral Neighbour Analysis Potential (SNAP)

The Spectral Neighbour Analysis Potential (SNAP) [30] calculates the density of neighbors in a spherically symmetric space that is centered around one atom. It also describes the interaction of atoms at higher orders (interaction terms with 3 atoms or more). The calculation of this descriptor begins with the neighbor density, which is defined as follows in Equation (2.15), as a sum of delta functions around a central atom i positioned at $\mathbf{R}$ in three-dimensional space.

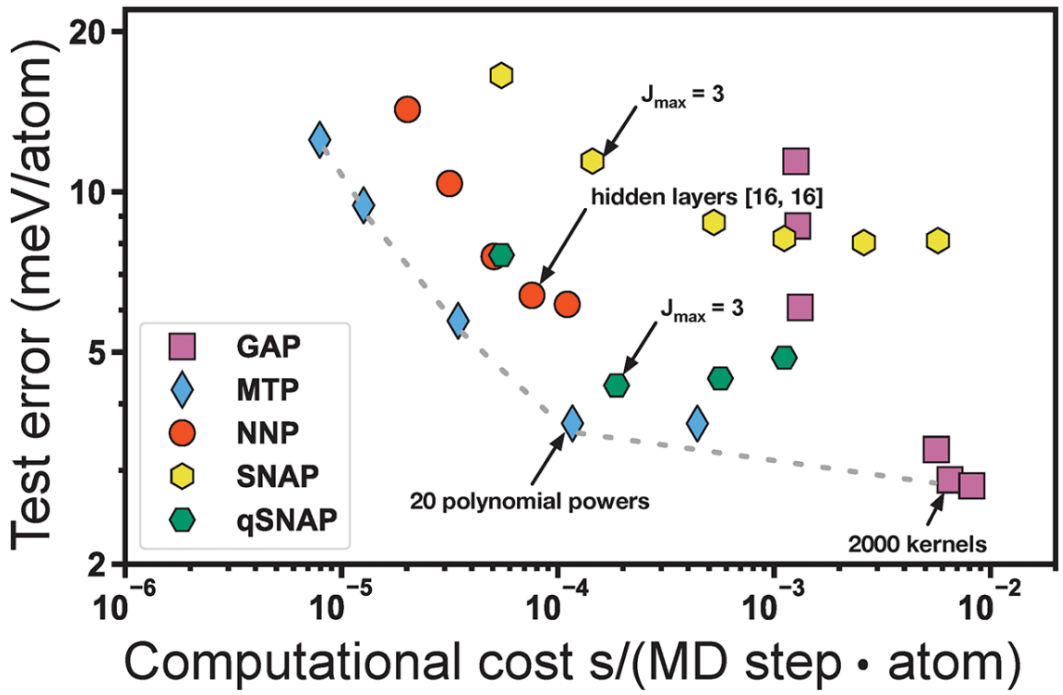

Figure 2.2: Plot of performance assessment of some of the available MLIPs found in literature, from Ref.[32]

$$\rho_i(\mathbf{R}) = \delta(\mathbf{R}) + \sum_{R_{ii'}<R_C} f_c(R_{ii'}) \cdot w_{i'} \cdot \delta(\mathbf{R} - \mathbf{R}_{ii'}) \tag{2.15}$$

where $\rho_i(\mathbf{R})$ is the neighbor density, $w_{i'}$ are dimensionless weights to distinguish atom types (species), $\mathbf{R}_{ii'}$ is the vector joining the position of the central atom i to the neighboring atom i', and $f_c(R_{ii'})$ is the switching functions that ensures that the contribution of each neighbor atom goes to zero at a distance of R_C.

The SNAP descriptors derived from $\rho_i(\mathbf{R})$ differ depending on the functions used to describe the angular and radial components. The one used in this study is the "SO(4) descriptor". Here, the components are formed upon a basis of 4D spherical harmonics and can be concisely represented as Equation (2.16). Here, $j = 0, \frac{1}{2}, 1, \ldots$ and $m, m' = -j, -j+1, \ldots, j-1, j$. Unlike the 3D spherical harmonics, here, the radial dimension is also mapped onto a third polar angle θ_0 and becomes periodic.

$$Y_j^{mm'} = f(\theta, \phi, \theta_0) \tag{2.16}$$

where *theta* is the polar angle and *phi* is the azimuthal angle.

Once we have the basis functions, the descriptor $D_i^{nmm'l}$ can be calculated by projecting the neighbor density ($\rho_i(\mathbf{R})$) onto the hyper-spherical basis functions described above. Equation (2.17) uses the Dirac notation to simplify the equation. Here, g_n is the radial basis.

$$D_i^{nmm'l} = \langle g_n Y_l^{mm'} | \rho_i(\mathbf{R}) \rangle \tag{2.17}$$

Once the descriptor is calculated for each form of neighbor interaction (pair, triplet, etc.) per atom, this can be then combined using a set of coefficients to calculate a net effective contribution by each atom (E_i) (Equation (2.18)). The value of j, which defines the limit of the values of m and m' as mentioned above, becomes a hyperparameter (to be set and converged during the calculation itself).

$$E_i = \sum_{nmm'l} \gamma^{nmm'l} \cdot D_i^{nmm'l} \tag{2.18}$$

Finally, the potential of the system (the end goal) is calculated using a linear combination of the effective contributions (E_i) (Equation (2.19)).

$$V(\mathbf{R}) = \sum_i E_i \tag{2.19}$$

Moment Tensor Potential (MTP)

The Moment Tensor Potential (MTP) [29] is a nonlinear potential unlike the SNAP potential mentioned above. This subsection goes into detail on how an MTP is calculated for a given configuration (cfg). Equation (2.20) shows that the potential energy of interatomic interaction ($E^{mtp}(cfg)$) is defined as a linear combination of the contribution by atom i in the neighborhood $\mathbf{n}_i$.

$$E^{mtp}(cfg) = \sum_{i=1}^{n} V(\mathbf{n}_i) \tag{2.20}$$

The function $V(\mathbf{n}_i)$ is expanded into a linear set of basis functions (B_α) as given in Equation (2.21) below.

$$V(\mathbf{n}_i) = \sum_\alpha \xi_\alpha B_\alpha(\mathbf{n}_i) \tag{2.21}$$

where $\xi = \{\xi_\alpha\}$ are parameters found from fitting to the training configurations. The next step is to define the moment tensor descriptors (or *moments* $M_{\mu,\nu}(\mathbf{n}_i)$) themselves, that are used to define the functional form of B_α. The moments have a radial and an angular component.

$$M_{\mu,\nu}(\mathbf{n}_i) = \sum_j f_\mu(|r_{ij}|, z_i, z_j) \underbrace{\mathbf{r}_{ij} \otimes \cdots \otimes \mathbf{r}_{ij}}_{\nu \text{ times}} \tag{2.22}$$

where f_μ are the radial functions, R_{ij} are tensors of rank ν and $\otimes$ defines a tensor outer product of vectors. z_i is the atomic type of the central atoms and z_j is the atomic type of the neighbouring atom. The radial function f_μ is defined between an R_{min} and R_{cut} that are the minimum distance and the cut-off distance for the interaction and is the term that makes the MTP nonlinear. The angular part, defined by the outer product of the tensors is hence of rank ν.

In order to construct B_α, the so-called *level* of moments is defined (Equation (2.23)).

$$\text{lev} M_{\mu,\nu} = 2 + 4\mu + \nu \tag{2.23}$$

The contraction of the levels is defined by the dot product (where the levels are added) and the Frobenius product (where the levels are multiplied). All such contractions are by definition invariant to rotations, atomic permutations, and reflections. Finally, a maximum level lev_{max} is used to include all the basis functions under the value of lev_{max}. How well the MTP performs hence relies on the tensors $\mathbf{r}_{ij}$, the number of different contractions (defined by lev_{max}), and the R_{cut}.

2.4.3 Training procedure for MLIPs

There is a specific procedure for training an MLIP. One needs to first create a dataset that the MLIP will be trained with. The dataset can be multiple different configurations of different sizes of supercells, or of the same supercell. Along with the configurations themselves, we also need the data on the energy and the forces acting on each of the atoms. The essential idea is to have a dataset that represents the potential energy surface (PES) of the given system, in a representative set of conditions (T, P). The MLIP is then trained using each of the configurations. In order to use it for Machine Learning, there are two major criteria that the dataset needs to fulfill - accuracy and large dataset size. In order to fulfill the former, it would be ideal to create new configurations that follow the canonical ensemble for the final potential that we need. In order to do this, once each configuration is created, we use the current entire dataset to retrain the MLIP, and then create a new configuration using this MLIP itself. In this manner, each new configuration is forced to follow our current best potential. As the data set size increases (for the latter), the MLIP represents the potential energy surface better and better.

2.4.4 MLACS

As one can imagine, there are many parameters that go into this procedure. Moreover, it takes time to perform each of the DFT energy/forces calculations on the configurations themselves. It would be an extremely taxing job to create new configurations and train the MLIP by feeding each configuration by hand. In order to facilitate this, we need an automated workflow. Dr. Aloïs Castellano [3] has created a Python package called Machine Learning Assisted Canonical Sampling (MLACS) that does exactly this. It interfaces *ab intio* software like Abinit [16] (that help calculate the energy/forces on the system) and the software LAMMPS [33] (which implements classical MD and the MLIP functional forms) to create new configurations using the iteratively trained MLIP. This makes it immensely easier to handle all the various parameters that go into the MLIP training. Figure 2.3 shows a simplistic flowchart of the procedure MLACS follows. MLACS is also interfaced with the Atomic Simulation Environment (ASE) [34, 35] that helps steer and analyze atomic simulations.

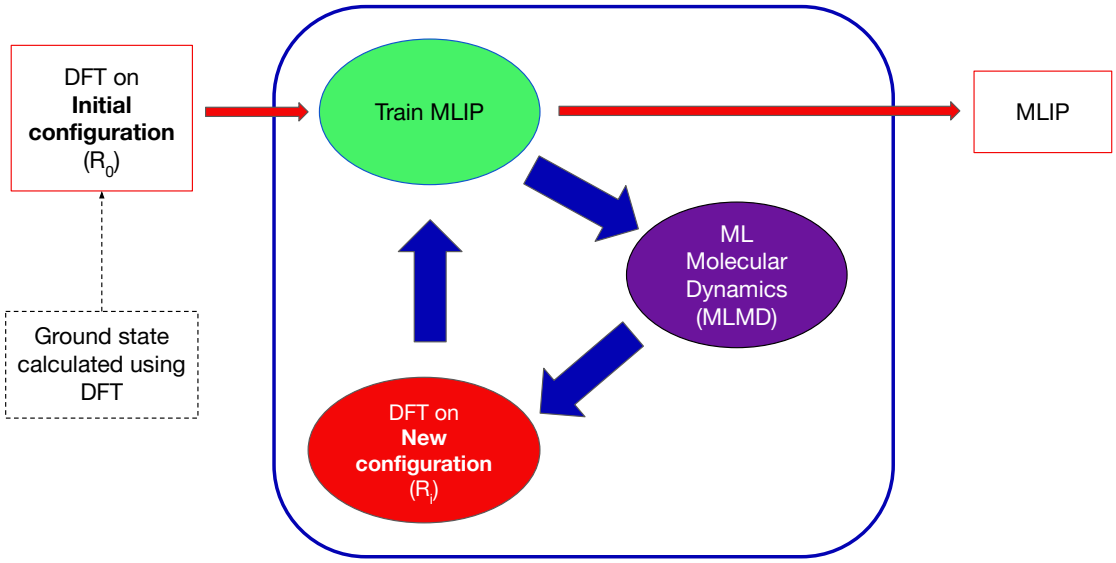

Figure 2.3: A flowchart of the sequence involved in creating an MLIP using MLACS

2.4.5 Finding the best hyperparameters

Each MLIP has its own set of hyperparameters that need to be intelligently chosen to produce the best possible MLIP. In an ideal scenario, the best MLIP is the one that gives the least error while also taking the least time to calculate

the energy/forces of a system. But, since we are creating an MLIP that has finite accuracy and should be able to handle very large systems, we must balance its speed vs accuracy. In order to compare multiple MLIPs, we perform what is called a *Gridsearch* algorithm. Here, we choose a set of values for each of the hyperparameters and train the MLIP using each of the combinations possible. The error is calculated using a testing set that is set aside from the global dataset when training. While the MLIP is being trained and tested, the amount of time taken for the MLIP to predict the data regarding a new configuration is also calculated (usually per atom). This now gives us an idea of how much time each of the hyperparameter combinations takes to predict the energy/forces of a new configuration as well as how accurate is it.

These values are then plotted on an 'Error vs Calculation Time' graph giving rise to what is called a *Pareto frontier*. (This is further discussed in Section 3.2). The MLIP that optimally fits our preference is then chosen and used for further calculations.

The results of the calculations and methods used in this section are presented in the next chapter.

3

Results and Discussion

The previous chapter elaborated on all the methods and kinds of calculations that were performed in this study. The objective is to be able to describe CDWs using the MLIPs generated using these methods. This chapter is essentially a detailed analysis of all the results of this study.

3.1 *ab initio* calculations using DFT

3.1.1 Groundstate convergence studies

As explained in Section 2.1.2, in order to calculate the energy of the ground state of a given material, multiple parameters need to be converged in order to save calculation time and achieve the required accuracy. Also, each of the MLIPs chosen have different hyperparameters that need to be optimized to get the fastest and the most accurate potential.

The high symmetry structures for monolayer 1T-$TiSe_2$ and 1T-TiS_2 were taken from the Materials Project [11]. These structures need to then be relaxed and have the parameters converged for the specific exchange-correlation functionals used.

For any kind of convergence study, there is always a tolerance value that needs to be considered. Based on the kind of properties that will be studied later on, the tolerance values are chosen. The tolerance value comes from experience and from a thorough scientific literature review. It is also known that DFT is an approximation and that is it not one hundred percent accurate. It hence has an intrinsic limit to its precision but is considered "absolute truth" for the MLIP fit. DFT involves several approximations - the potential energy surface considered is that obtained in the Born-Oppenheimer approximation, the exchange correlations functionals are approximations and the SCF (Self Consistent Field) cycles have their own tolerance. Also, simulations are performed on perfect crystals which are

approximations of true materials in physical experiments. Moreover, the MLIP that is being fit on the configurations also has a limit on its accuracy. We hence use a tolerance of a difference of 1 $meV/atom$ in the energy of the system that is calculated. Mathematically it is represented as follows.

$$Total\ Energy_n - Total\ Energy_i < 1meV\ per\ atom \tag{3.1}$$

where n is the highest value (usually chosen such that the value is over-converged) and i is the index of the variable at which the $Total\ Energy$ is being calculated. The difference in energies defined above in Equation (3.1) is converged within the aforementioned tolerance value.

Convergence of kinetic energy of the pseudopotential

The pseudopotentials used are norm-conserving and work with the Perdew-Burke-Ernzerhof (PBE [19]) functional, which is a GGA exchange-correlation functional. They were taken from the Pseudo-Dojo website [36].

The cutoff values that were used for studying the convergence are `{10,15,25,35,45,55,65,100}` Hartree. The SCF cycles converged to a difference in total energy of the system of 1^{-10} Hartree between two iterations.

Figure 3.1 is a plot describing the convergence of the kinetic energy cutoff imposed on the pseudopotential, that defines the number of plane waves included in the basis set, hence affecting the accuracy and efficiency of the calculation. As explained above in Equation (3.1), the tolerance of 1 $meV/atom$ is applied to find the converged cutoff value. The monolayer 1T-$TiSe_2$ converged with a cutoff of 50 Hartree and 1T-TiS_2 with a cutoff of 45 Hartree. Although any value above these can be chosen, the improved accuracy is not necessary.

Convergence of size of *k*-point size and electronic temperature

Figure 3.2 and Figure 3.3 show the convergence of k-point grid size (as explained in Section 2.1.1) along with the electronic temperature for both the materials. When the k-point grid size is limited, discretization of the reciprocal space might not accurately capture the electron occupation around the Fermi level. Adding a "smearing" temperature increases the width over which the electrons can be smeared, smoothing out the k-points. A statistical model of a thermodynamical ensemble is used to populate the electrons in those bands. In order to increase the speed of the calculation, we do both to find a balance between the electronic temperature given and the density of the k-point grid used. Even in this case, the same tolerance of 1 $meV/atom$ (as mentioned in Equation (3.1)) is used.

The values of k-points grid size (square grids - $n \times n$) used are `{10,12,14,16,18,20,24,28,40}`, for smearing temperatures (in Kelvin) of

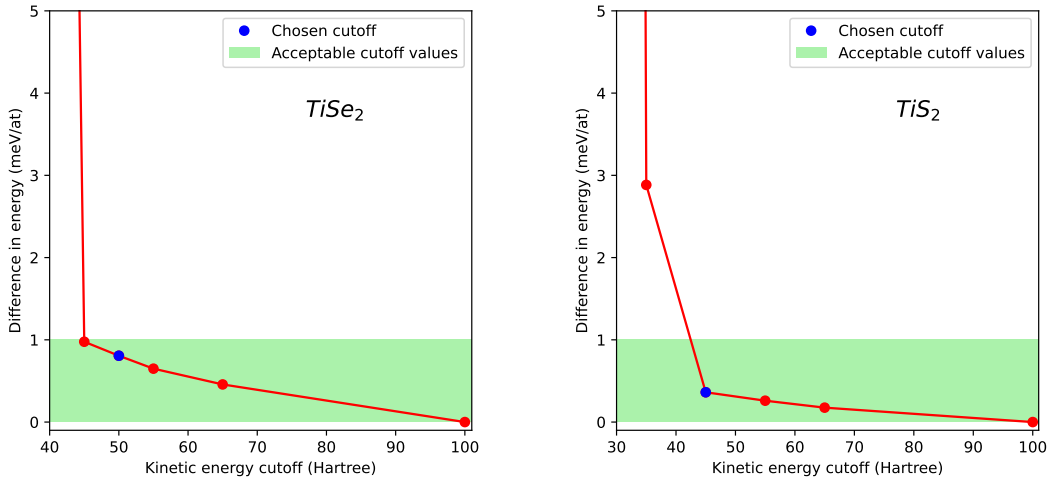

(a) (b)

Figure 3.1: Plot of difference in energy vs the kinetic energy imposed on the plane wave basis set for (a) monolayer 1T-$TiSe_2$ and (b) monolayer 1T-TiS_2

`{1.16,5.80,11.60,58.02,116.04,580.22,1160.45}` (the same in eV are `{0.0001,0.0005,0.001,0.005,0.01,0.05,0.1}`).

From Figure 3.2(b), it can be easily concluded that the plot for 1T-TiS_2 has converged (reached the tolerance level) very quickly as compared to 1T-$TiSe_2$. This could be because of the band gap that is visible in the groundstate electron band structure of 1T-TiS_2, which makes it an insulator. Since insulators do not have electron occupation above the Fermi level, they could be insensitive to higher temperature smearing.

Convergence of interlayer distance

A monolayer consists of a single layer of material. Yet, as mentioned earlier, DFT uses periodic boundary conditions as it does the calculations in the reciprocal space. This means that even a monolayer will be replicated indefinitely. Instead, we can increase the size of the cell parameter in the z direction such that the interaction between the repeated layers will come to a minimum and will hence be treated as a monolayer. We not only lack the necessary computational capacity to accommodate an infinitely large cell size, but our requirement is only a monolayer. We hence need to converge this parameter using the same tolerance value used above. Figure 3.4 shows the above-mentioned convergence plot. This ensures that the material we are working with is an isolated monolayer.

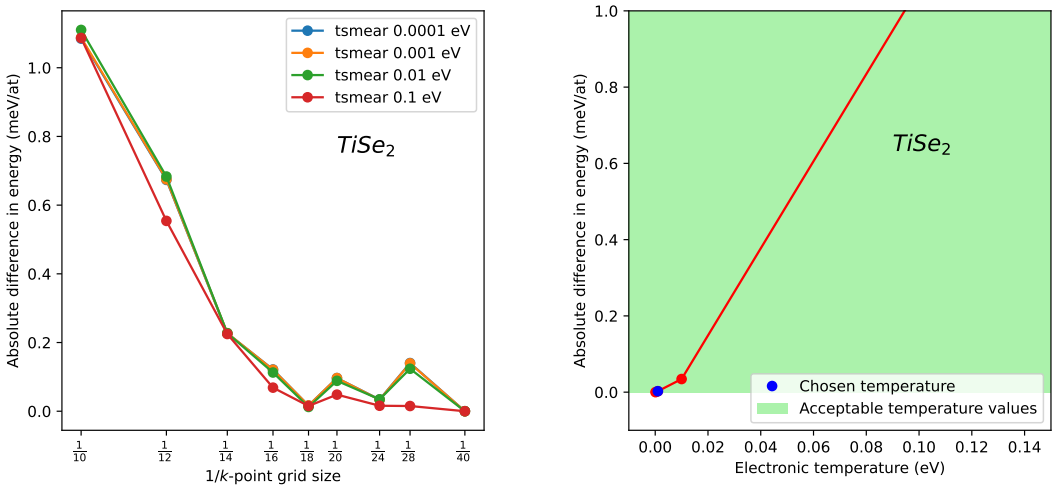

(a) (b)

Figure 3.2: (a) Plot of convergence of difference in energy vs k-point grid size, with change in electronic temperature (for monolayer 1T-$TiSe_2$); (b) Plot of difference in energy vs electronic temperature at each converged k-point size

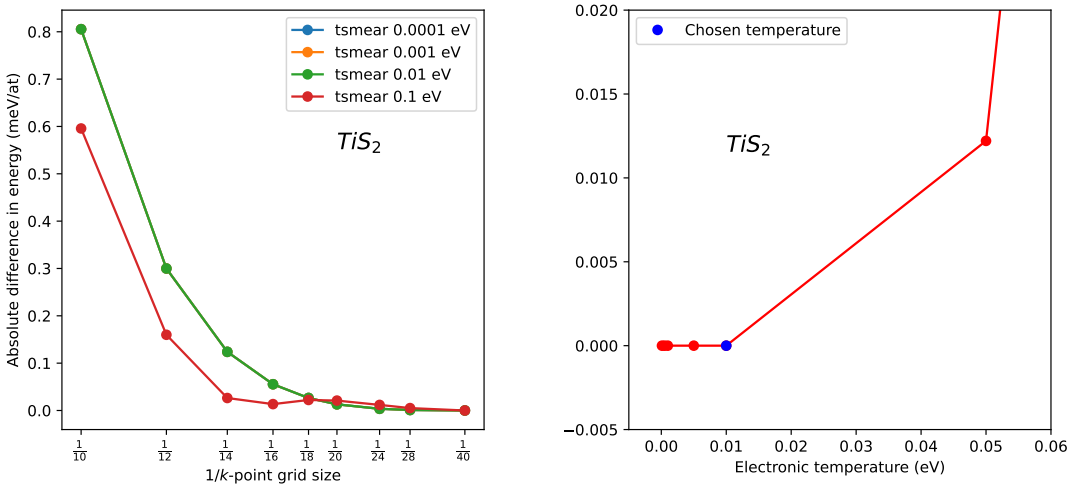

(a) (b)

Figure 3.3: (a) Plot of convergence of difference in energy vs k-point grid size, with change in electronic temperature (for monolayer 1T-TiS_2); (b) Plot of difference in energy vs electronic temperature at each converged k-point size

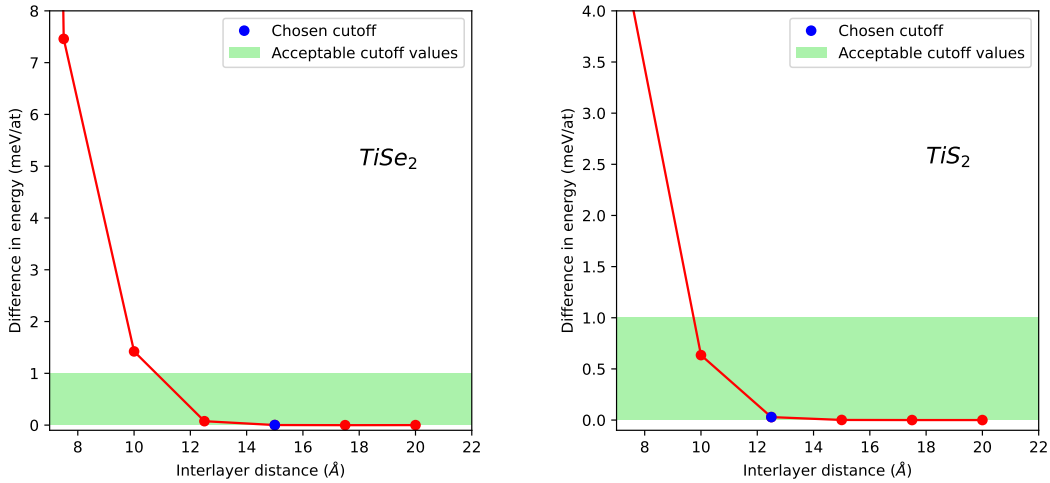

(a) (b)

Figure 3.4: Plot of interlayer distance convergence for (a) monolayer 1T-$TiSe_2$ and (b) monolayer 1T-TiS_2

3.1.2 Electronic band structures

As explained in Section 1.1.1, CDWs are associated with a second-order phase transition from an insulator phase (below T_{CDW}) to a metallic phase (above T_{CDW}). It is hence of utmost importance to plot the electronic band structures of the high symmetry phase to understand the electron bands and their occupation around the Fermi level. The material has to ideally be a metal in its high symmetry phase. A major factor that affects the bandgap in simulations is the exchange-correlation (xc) functional used. For example, the Local Density Approximation (LDA) and the Generalized Gradient Approximation (GGA) xc functionals are known to underestimate the band gap strongly.

We chose to use the PBE-GGA xc functional [19] based on a review of the available literature. For the case of 1T-$TiSe_2$, it has been shown that using the LDA xc functional, the theoretical cell of the system does not display any instability [2], while on the other hand, using the PBE-GGA xc functional (correctly) displays a large phonon instability at the M point of the Brillouin zone [2, 37]. Additionally, the use of the LDA+U functional led to an increase in the phonon frequency (thereby making it more stable) with an increase in U correction. For the case of 1T-TiS_2 as well, the LDA+U correction did not display any instability (no CDW phase) [4]. The use of the modified Becke-Johnson functional (mBJLDA) [4] gave a good estimation of the bandgap.

Given this background we concluded that it made sense to first choose the PBE-GGA functional [19] and calculate the electron band structure, following which, the energies and forces of supercells (to be run using MLACS) are calculated. Shown in Figure 3.5 are the electron band structures for both monolayer 1T-$TiSe_2$ and monolayer 1T-TiS_2, calculated using the GGA *xc* functional. It is quite clear from Figure 3.5(a), that 1T-$TiSe_2$ is a metal since there is no band gap at all. On the other hand, 1T-TiS_2 (Figure 3.5(b)) presents a very small bandgap of 0.0737 eV. These calculations were performed with the addition of electronic temperature to ensure the physically correct occupation of electron bands around the Fermi level. A temperature of only 11.60K (0.001 eV) was used for the monolayer 1T-$TiSe_2$, while a higher temperature of 116.04K (0.01 eV) was used for the monolayer 1T-TiS_2. Yet, there was a bandgap only for the latter. This means that 1T-TiS_2, even within the GGA approximation (we know that it underestimates the band gap), presents a semiconducting phase.

According to the experiments, the bandgap of bulk 1T-$TiSe_2$ is about 0.045 eV at room temperature, and the transition to a higher band gap phase occurs at 200K [38]. But there is not much data available for the monolayer 1T-$TiSe_2$.

In order to look at the effects of the *xc* functional on the band gap of 1T-TiS_2, we further calculated the electron band structures using two other meta-GGA functionals. We first used the modified Becke-Johnson (mbJ) exchange functional [39] in combination with the PW-LDA [40] correlation functional. Here, the ground state structure was imported from calculations with the PBE-GGA [19] functional. We then used the re-regularized SCAN (Strongly Constrained and Appropriately Normed) exchange functional by Furness et al in combination with the re-regularized SCAN correlation functional [41, 42] (with larger value for eta). Figure 3.6(a) and (b) show the electron band structures for monolayer 1T-TiS_2 when using the above described mBJ and SCAN functionals respectively. The bandgaps calculated were 0.0756eV and 0.7538 eV for the mBJ and SCAN functionals respectively. The SCAN functional has clearly overestimated the bandgap value (as compared to the literature, which shows values between 0.05 to 2.5eV [43, 44]).

Since we know that CDWs exist in both the materials in their low temperature states, it would be ideal to see a metallic phase from their electron band structures. The PBE functional looks satisfactory, but the mBJ functional might be more apt to our study. Given the successful demonstration of CDWs in both the materials using the GGA functional and the availability of a substantial dataset for comparative analysis, we chose this functional for all the DFT calculations in the rest of the study.

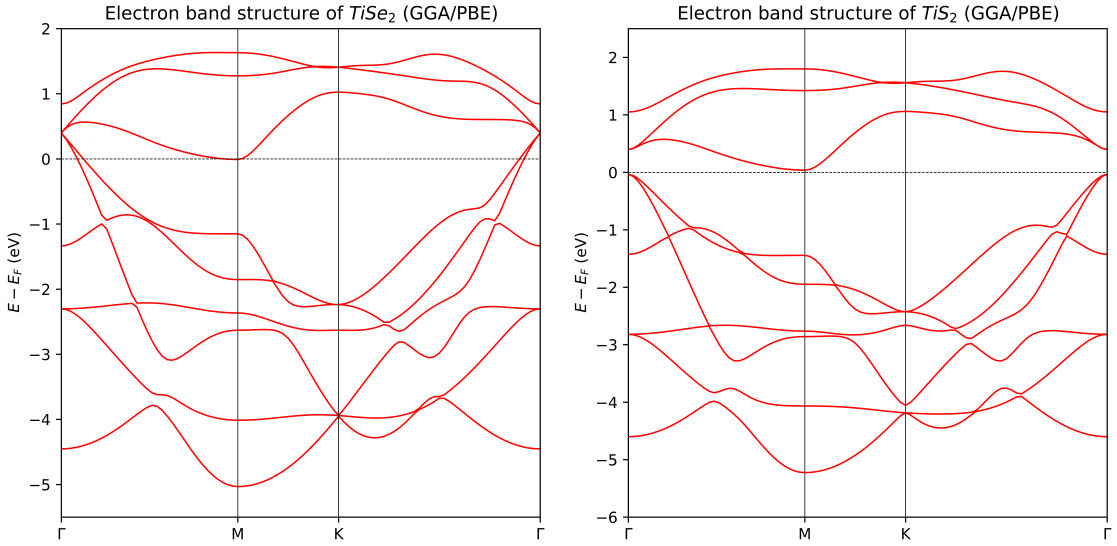

(a) (b)

Figure 3.5: Plot of the electron band structure calculated using the PBE pseudopotential for (a) monolayer 1T-$TiSe_2$ and (b) monolayer 1T-TiS_2

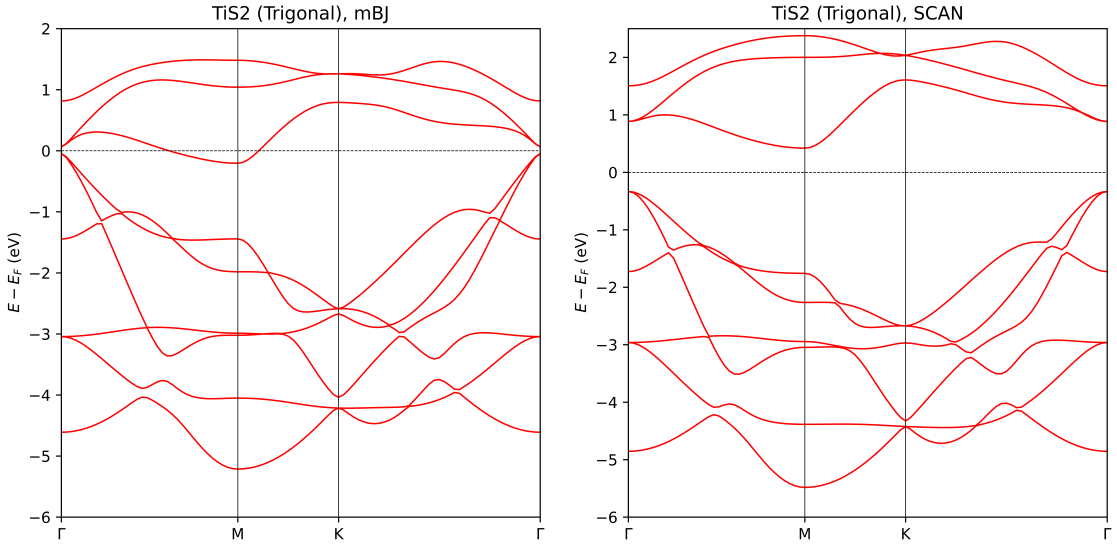

(a) (b)

Figure 3.6: Plot of the electron band structure calculated using the (a) mBJ and (b) SCAN pseudopotential for monolayer 1T-TiS_2

3.2 Finding the best MLIP parameters

In Section 2.4.5, we discussed how the best MLIP is chosen in a given family. In short, We train the MLIP on different combinations of hyperparameters and then plot them on an 'Error vs Calculation Time' graph. Shown in Figure 3.7 and Figure 3.8 are such plots for the two chosen MLIPs (namely SNAP and MTP) for $TiSe_2$ and TiS_2 separately. It can be clearly seen that there is a specific border (a curve) in the plot, above which the graph is populated. This curve (as represented in the graph) is called the *Pareto frontier*. It is a convex curve that shows the optimal balance between the time and accuracy of each MLIP. If we move away from the frontier into the region inside, we do not gain any increase in accuracy for the given increase in calculation time. The ideal hyperparameter set is usually picked when the error is converged - meaning, with an increase in calculation time, there is only a minute reduction in the error and we are at the limits of the underlying MLIP functional form. Shown in Table 3.1 and Table 3.2 are the final hyperparameters chosen for the potentials, for each of the materials.

The error was defined as a linear combination of errors on the energy, forces, and stress, as given in Equation (3.2). The different coefficients help weigh the error that is most important for the required calculation (energy, force or stress) by magnifying its contribution.

$$Error(\Delta) = \sigma_1 \cdot RMSE_{energy} + \sigma_2 \cdot RMSE_{forces} + \sigma_3 \cdot RMSE_{stress} \tag{3.2}$$

where $RMSE$ is the Root Mean Square Error between the values calculated by the MLIP and those given by the *ab initio* DFT.

Following are the hyperparameters and all of their values that were used in the grid search of the MLIPs.

3.2.1 Hyperparameters for the SNAP potential

- **chemflag** - Toggle variable whether to or not consider the different chemical species around a given atom. If off, all atoms would be weighted equally. The values can be `{0 or 1}`.
- $\mathbf{R_{cut}}$ - The radius within which neighboring atoms are considered for a given central atom. The values considered were `{4.0,4.2,...,6.0}` in Angstrom. These values were chosen after studying the inter-atomic distances and the size of the supercell used for the DFT calculations.
- $\mathbf{2J_{max}}$ - The maximum value of the parameters m and m' chosen for the angular basis set (spherical harmonics in 3D). The values considered were `{5,6,7,8}`. It was observed that a $2J_{max}$ value of 7 already gave the same order of accuracy as a $2J_{max}$ of `8`. Hence, we stopped at `8`.

- **training ratio** - The dataset of configurations is divided into a training and testing set. The MLIP is first fit on the training set and then tested on the testing set. The *training ratio* is hence the ratio of number configurations considered for training, to the total number. The values considered for the training ratio were `{0.7,0.8,0.9}`.

- **number of splits into train and test sets** - It is not enough to split the configurations set once. Multiple random splits ensure that the MLIPs are not overfitted on similar configurations and hence learn the full Potential Energy Surface (PES). The value chosen was `5`, as there was very little change observed, onc changing the test and train sets.

3.2.2 Hyperparameters for the MTP potential

- $\mathbf{R_{cut}}$ - Similar to the SNAP potential, the values considered are `{4.0,4.6,...,7.4}` in Angstrom, based on the supercell size.

- $\mathbf{lev_{max}}$ - The number of different contractions of the moments calculated (as explained in Section 2.4.2). The values considered were `{14,18,22,24}`. A *level* of 18 already gave the same order of accuracy as the higher ones.

- **training ratio** - As with the SNAP potential, the values chosen are `{0.7,0.8,0.9}`.

- **number of splits into train and test sets** - Unlike the SNAP potential, the chosen value here is `4`, since the MTP takes slightly longer for the calculation of the MLIP.

As mentioned above, in the Figure 3.7 and Figure 3.8, the points represented in red form the *Pareto frontier*. From these points, we choose the one at the inflection point where the frontier becomes much flatter. It is visible from these figures that MTP potentials are more accurate: most of the data points for the MTP potentials lie near the *Pareto* frontier as well, showing stability with changes in parameters.

It is also important to mention that the calculation times are all very small. Even if we choose the MLIP with the longest calculation time, we still end up nowhere near the time taken to calculate the energy/force using *ab inito* methods such as DFT. This is a clear win for MLIPs. To compare the time taken for the MLIP calculations, we used a serial version of LAMMPS for both SNAP and MTP. Figure 3.7 and Figure 3.8 show that the SNAP potential is definitely faster at calculating the energy, the forces, and the stress on the system as compared to the MTP potential.

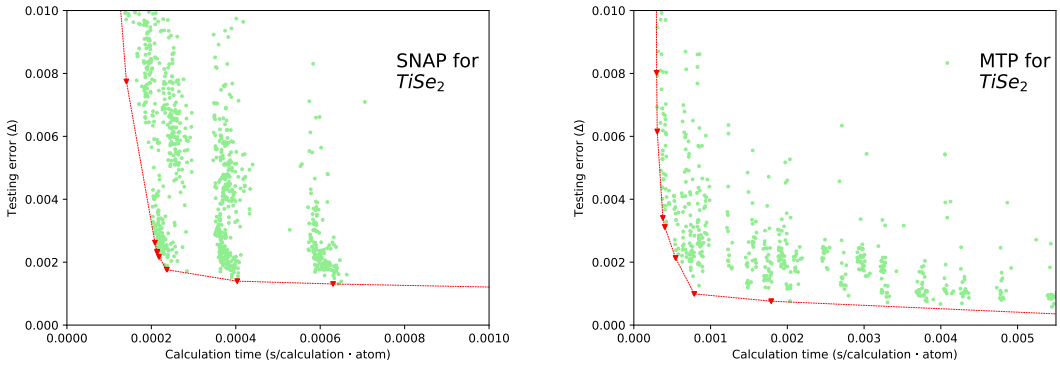

(a) (b)

Figure 3.7: Plot of accuracy vs calculation time when using different hyperparameters for (a) SNAP potential and (b) MTP potential, for monolayer 1T-$TiSe_2$

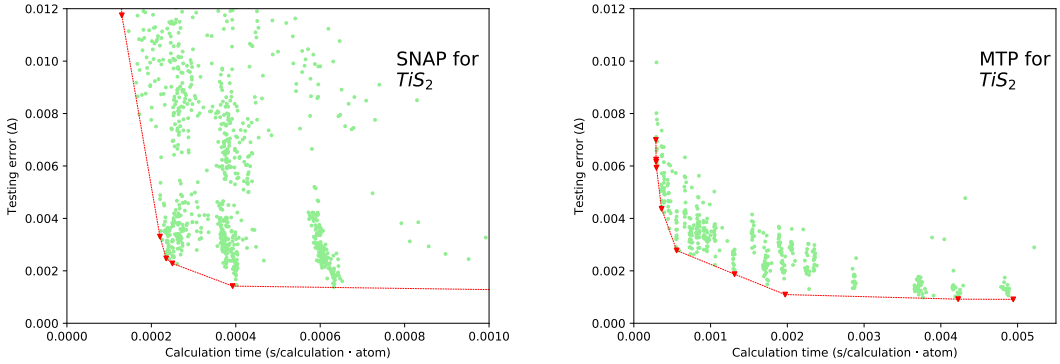

(a) (b)

Figure 3.8: Plot of accuracy vs calculation time when using different hyperparameters for (a) SNAP potential and (b) MTP potential, for monolayer 1T-TiS_2

Figure 3.9 and Figure 3.10 show the correlation plots between the forces calculated by DFT and the MLIP, for the SNAP and MTP potentials respectively, on data previously unseen by the MLIP (test set). They show very good R^2 (coefficient of determination) errors with values very close to 1. Correlation plots are hence a very good measure of how well the MLIP learns from the provided DFT configurations.

Hyperparameters	**1T-$TiSe_2$**	**1T-TiS_2**
chemflag	1	1
R_{cut} (Å)	5.8	5.8
$2J_{max}$	6	8
Training ratio	0.8	0.9

Table 3.1: Final parameters chosen for the SNAP potential

Hyperparameters	**1T-$TiSe_2$**	**1T-TiS_2**
level	18	18
R_{cut} (Å)	7.0	7.0
Training ratio	0.9	0.9

Table 3.2: Final parameters chosen for the MTP potential

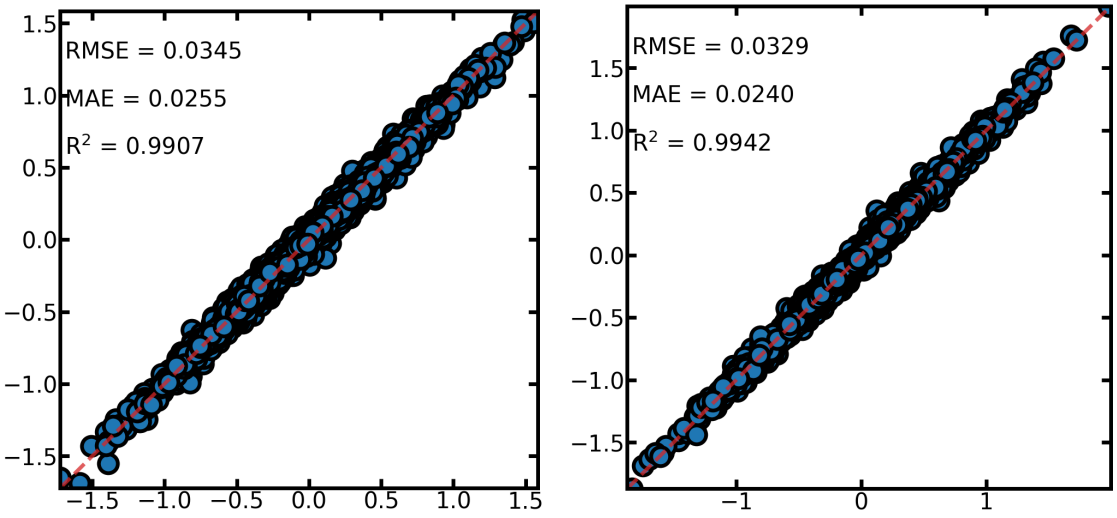

(a) (b)

Figure 3.9: Correlation plot for the forces calculated by DFT and the chosen SNAP potential, for (a) monolayer 1T-$TiSe_2$ and (b) monolayer 1T-TiS_2

3.3 MLIP predicts the CDW

The previous sections dealt with all the steps that go into creating the MLIP, namely - generating the first principles ground state geometry and electronic structure with the *xc* functional (PBE-GGA). The rest of this chapter will deal with

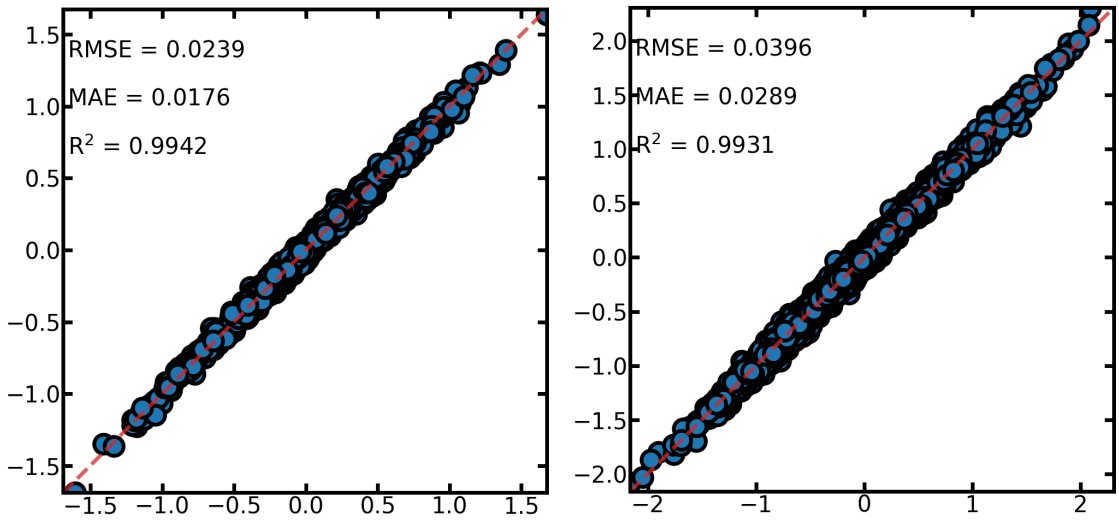

(a) (b)

Figure 3.10: Correlation plot for the forces calculated by DFT and the chosen MTP potential, for (a) monolayer 1T-$TiSe_2$ and (b) monolayer 1T-TiS_2

the results obtained from performing calculations using MLIPs that are fit these first principles results. Specific tests, namely - checking for physical distortion and checking for the instability at the M point (*Kohn anomaly*) have been performed to check the sensitivity of the MLIPs created. Since CDWs are a quantum phenomenon, it is expected that a classical potential might not be able to fully describe the process.

3.3.1 Ground state structure using the MLIPs

Using the MD package LAMMPS, an energy minimization was performed on a 10 × 10 supercell for both materials. Since the high symmetry phase is already in an equilibrium state with all the internal forces nullified, the supercell first needs to be distorted a little by giving all the atoms random (but not too large) displacements. Following this, the supercell is allowed to relax and find a stable energy minimum using the *conjugate-gradient* method. This is done by using the LAMMPS command `minimize`. The relaxed structures, using the MTP MLIP are presented in Figure 3.11. They show a very clear PLD that is a positive sign of the presence of a CDW (as explained in Section 1.1.1).

In Section 3.2, we showed that the MTP potential is more accurate than the SNAP potential and hence we have made calculations mainly with the MTP potential.

As it is now clear that the MLIPs can predict the lattice distortion, the next

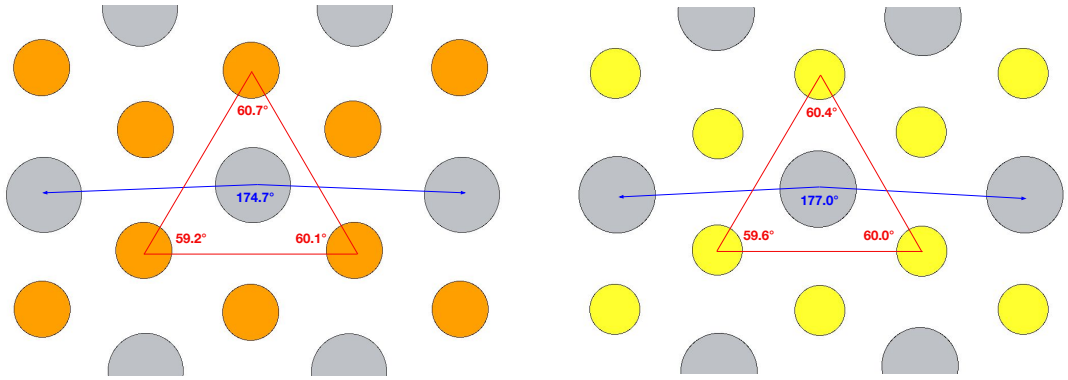

(a) (b)

Figure 3.11: Schematics showing the periodic atomic distortion depicting values of angular distortion in (a) monolayer 1T-$TiSe_2$ (gray atoms are Ti and orange Se) and (b) monolayer 1T-TiS_2 (gray atoms are Ti and yellow S).

step is to look at whether this instability can be predicted with the use of phonon dispersion curves.

3.3.2 Phonons calculated using finite-difference method

Figure 3.12 shows plots of the phonon dispersion curves calculated using the finite difference method as explained in Section 2.3.2. Each plot shows three curves. The black dotted curve represents the phonons calculated using the data received directly from DFT calculations. The blue curve is calculated using the SNAP potential and the red, using the MTP potential. As discussed in Section 2.3.2, phonons calculated using the finite difference do not take into consideration the temperature effects.

For both materials, the phonons calculated from the DFT data are very similar to those from the literature [4, 37, 45] (as shown in Figure 1.3 [1]). They show a very strong instability at the M point of the Brillouin zone (as shown in Figure 1.3(b)), pointing to the *Kohn anomaly*. This once again confirms that the exchange-correlation functional chosen does indeed produce a CDW. The results of the previous section (Section 3.3.1) make it clear that upon relaxation with the MLIP, the atoms do find the energy minima corresponding to the CDW state. Yet, in the case of 1T-$TiSe_2$, the phonons calculated (using the finite-difference method) using both SNAP and the MTP (Figure 3.12(a)) do not predict the instability, meaning the high symmetry phase is (at least meta) stable.

For the case of 1T-TiS_2 (Figure 3.12(b)), although the frequency of the unstable phonon is not as high as the DFT calculated phonon, both the MTP and SNAP

MLIPs manage to show an instability, confirming the existence of the CDW in the MLIP potential energy surface.

The difference in instability between the two materials is quite puzzling. A quick look at the electron band structures calculated using the GGA functional (Section 3.1.2) shows us that monolayer 1T-$TiSe_2$ is a metal in its high symmetry groundstate while monolayer 1T-TiS_2 is a semiconductor. The CDW phase transition on the other hand is defined by a semiconductor (CDW phase) to metal transition (high symmetry phase), and hence it is 1T-$TiSe_2$ that should be showing the stronger instability.

The instability shown by the MLIPs for monolayer 1T-$TiSe_2$ is also very small as compared to the groundstate DFT calculation. This is most likely due to the limitation of the accuracy of these potentials, wherein they are unable to describe sensitive phenomena like CDW phase transitions. The above-drawn conclusion is based on the fact that there have been no dynamics run to calculate the phonons, but instead, it solely relies on the forces and their derivatives calculated by our own potential. If the potential has learned the quantum effect, it should surely show up here.

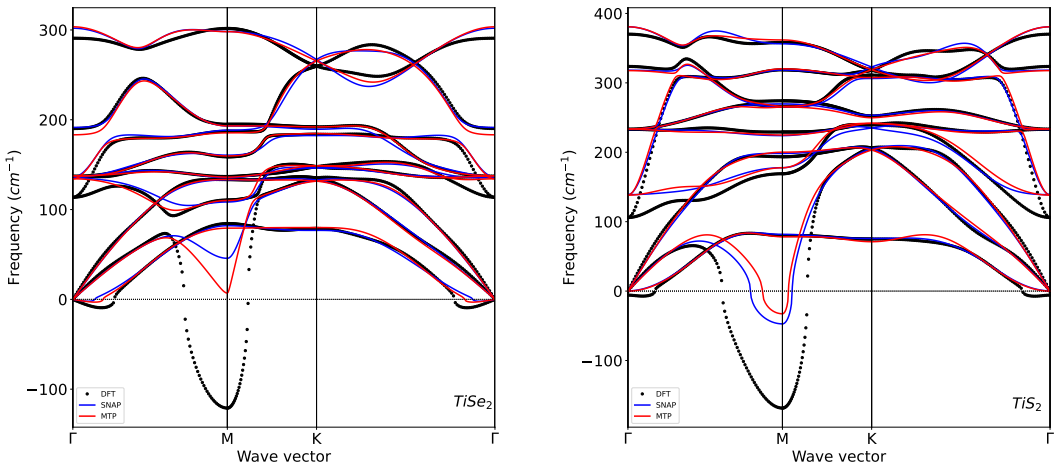

(a) (b)

Figure 3.12: Phonon dispersion curves calculated using the harmonic approximation and finite-difference method for (a) monolayer 1T-$TiSe_2$ and (b) monolayer 1T-TiS_2

3.3.3 Temperature dependent phonons using TDEP

As explained in Section 2.3.3, we use the anharmonic lattice dynamics theory called TDEP to calculate the temperature-dependent phonons using our MLIPs. Figure 3.13 shows the phonon dispersion curves calculated over a range of temperatures (50K to 600K) for both materials. Based on whether or not the CDW exists at a particular temperature, the instability (phonon frequency) at the M point will vary. If the transition temperature (T_{CDW}) lies in the range of temperatures chosen, the phonon frequency should show a clear shift from an imaginary to a positive value (as shown in literature Figure 1.3).

As explained in Section 2.3.3, there are multiple steps taken to calculate the phonons using TDEP. In short, TDEP requires a unit cell (with a cell size taking thermal expansion into account), and a distribution of configurations pertaining to the canonical ensemble, for each temperature. The unit cell needs to be of the high symmetry phase in order to make sure that TDEP is able to define the M-point instability well.

In neither of the Figure 3.13(a) or (b), do we see a phase transition down to 50 K. There is definitely a strong dependence of the phonons on temperature, particularly at the M point, as we see the phonon softening with reducing temperature, but no destabilization.

There are multiple variables that can be tuned in the TDEP calculations. One such variable is the first-order force constant correction, which corrects the reference atom positions to obtain the finite temperature equilibrium structure. An alternative to this correction is to fit the expansion in cell size for different temperatures with a function and then interpolate to whichever temperature is required. Both of these methods were tested with very similar results, with neither describing the phase transition accurately. This could mean two things: the chosen MLIPs - SNAP and MTP are either not sensitive to quantum phenomena like CDWs (meaning they are unable to accurately reproduce DFT data) and hence require more accurate potentials like Neural Network Potentials (NNP). Or, the hyperparameters chosen for the MTP gridsearch (Section 3.2) are not accurate enough, and interactions over a longer range need to be considered.

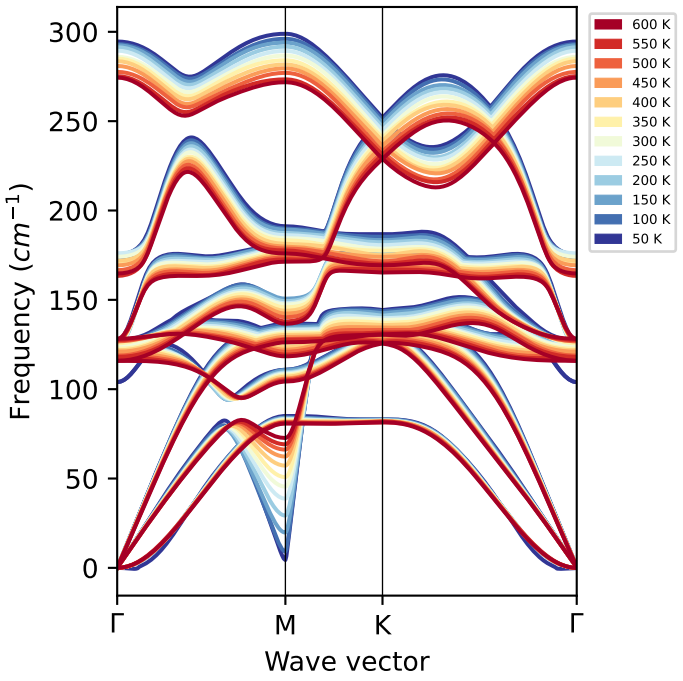

(a)

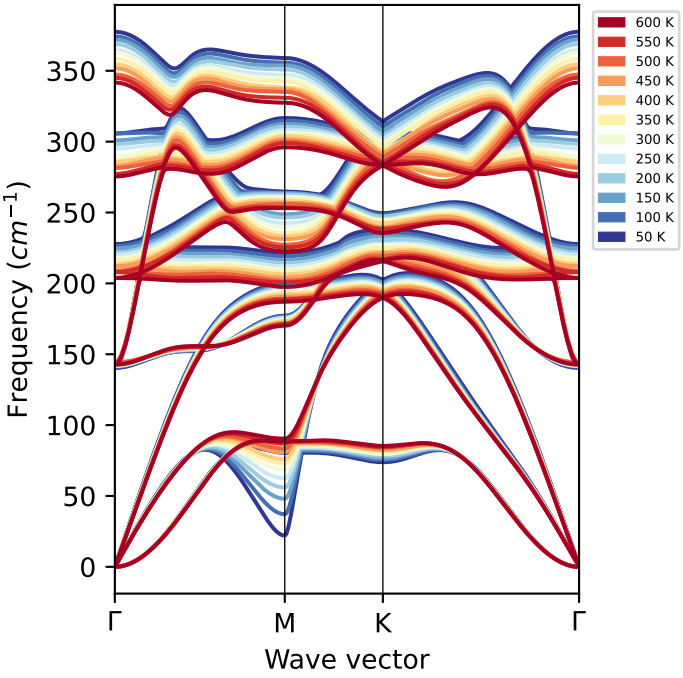

(b)

Figure 3.13: Phonon dispersion curves calculated using TDEP for (a) monolayer 1T-$TiSe_2$ and (b) monolayer 1T-TiS_2

4 Conclusions

In summary, this Master's thesis presents a comparison of the speed and accuracy between two MLIPs - SNAP and MTP, to check if they can successfully predict the second order phase transition seen in the two monolayer TMDs - 1T-$TiSe_2$ and 1T-TiS_2 chosen for this study. MLIPs are extremely fast as compared to AIMD simulations. We have shown that the calculation times (per atom) are in the order of milliseconds, and can hence be used for large systems and long MD integration times, and in combination with techniques like TDEP to calculate material properties.

It was initially concluded that the PBE-GGA exchange-correlation functional could predict the band gap with enough accuracy, especially because of the already available literature and scientific data. However, since the phonon dispersion curves did not give us the desired properties, the choice of the functional definitely has to be revisited. The groundstate of the two materials was calculated using DFT and the MLIPs were then trained using the package MLACS. The MLIP hyperparameters were tuned and the SNAP and MTP potential were compared. We also showed that the MTP potential is more accurate than the SNAP potential. An anharmonic theory (TDEP) was then used to calculate the temperature-dependent phonons for both materials.

The MLIP/DFT correlation plots also show that they are quite accurate at predicting the forces on the atoms, energies, and stress. This has been demonstrated by running MD simulations where the system transitions to the CDW state when relaxed. The MLIP supercells show a clear Periodic Lattice Distortion (PLD), a clear sign of the CDW phase. However, phonon dispersion curve calculations on the other hand gave us conflicting results. Finite difference calculations predicted the existence of the CDW for monolayer 1T-TiS_2 and not for 1T-$TiSe_2$. This is a clear sign of inaccuracy of the MLIPs as there are no other dynamics at play. If the MLIPs were able to predict the CDW for 1T-TiS_2, it means that they most

likely need to be tuned better for the case of 1T-$TiSe_2$.

Phonons calculated using TDEP on the other hand showed no instability at the M point down to 50K, even for 1T-TiS_2. This leads us to conclude once again that the MLIPs fit on our data were not able to reproduce the DFT data accurately enough to predict the CDW. In the case of TDEP, the quantum level information that might be hidden in the MLIPs should be visible, because of the molecular dynamics that were performed during the calculations. Although we see a PLD during the MD test, we do not see the unstable phonon in this case.

In conclusion, the MTP and SNAP potentials that were fit on our data were not accurate enough to reproduce the same instability seen in the scientific literature. The use of more accurate hyperparameters or of better potentials like NNP (albeit at a higher computational cost) needs to be carried out and compared to the results of this thesis. On the whole, these potentials can be used for classical MD simulations as they were indeed able to predict the groundstate of the CDW phase for both the materials. Once the MLIP learns the CDW instability, it can be used to calculate material properties such as thermal conductivity. Hereto, from all the observations made, it can be inferred that a study of the effect of other exchange-correlation functionals that can be used in place of the GGA functional for the DFT "ground truth", will shed light on whether the functional plays a major role in the final MLIP produced.

Bibliography

[1] Jianqiang Sky Zhou et al. "Anharmonicity and Doping Melt the Charge Density Wave in Single-Layer TiSe2". In: *Nano Letters* 20.7 (2020). PMID: 32496779, pp. 4809–4815. DOI: 10.1021/acs.nanolett.0c00597.

[2] Raffaello Bianco, Matteo Calandra, and Francesco Mauri. "Electronic and vibrational properties of TiSe2 in the charge-density-wave phase from first principles". In: *Physical Review B - Condensed Matter and Materials Physics* 92 (9 Sept. 2015). ISSN: 1550235X. DOI: 10.1103/PhysRevB.92.094107.

[3] Alois Castellano et al. "*Ab* initio canonical sampling based on variational inference". In: *Phys. Rev. B* 106 (16 Oct. 2022), p. L161110. DOI: 10.1103/PhysRevB.106.L161110.

[4] Kapildeb Dolui and Stefano Sanvito. "Dimensionality-driven phonon softening and incipient charge density wave instability in TiS2". In: *EPL* 115 (4 Aug. 2016). ISSN: 12864854. DOI: 10.1209/0295-5075/115/47001.

[5] O. Hellman and I. A. Abrikosov. "Temperature-dependent effective third-order interatomic force constants from first principles". In: *Phys. Rev. B* 88 (14 Oct. 2013), p. 144301. DOI: 10.1103/physrevb.88.144301.

[6] Ritu Gupta et al. "A brief review of the physical properties of charge density wave superconductor LaPt2Si2". In: *Superconductor Science and Technology* 35 (8 Aug. 2022). ISSN: 13616668. DOI: 10.1088/1361-6668/ac7755.

[7] Xuetao Zhu et al. *Misconceptions associated with the origin of charge density waves*. May 2017. DOI: 10.1080/23746149.2017.1343098.

[8] Hong Wang et al. "Large-Area Atomic Layers of the Charge-Density-Wave Conductor TiSe2". In: *Advanced Materials* 30 (8 Feb. 2018), p. 1704382. ISSN: 1521-4095. DOI: 10.1002/ADMA.201704382.

[9] C. H. Chen et al. "Angle-resolved photoemission studies of the band structure of $TiSe_2$ and TiS_2". In: *Phys. Rev. B* 21 (2 Jan. 1980), pp. 615–624. DOI: 10.1103/PhysRevB.21.615.

[10] A. H. Thompson, K. R. Pisharody, and R. F. Koehler. "Experimental Study of the Solid Solutions $Ti_xTa_{1-x}S_2$". In: *Phys. Rev. Lett.* 29 (3 July 1972), pp. 163–166. DOI: 10.1103/PhysRevLett.29.163.

[11] Logan Ward et al. "A general-purpose machine learning framework for predicting properties of inorganic materials". In: *npj Computational Materials 2016 2:1* 2 (1 Aug. 2016), pp. 1–7. ISSN: 2057-3960. DOI: 10.1038/npjcompumats.2016.28.

[12] Ghanshyam Pilania et al. "Accelerating materials property predictions using machine learning". In: *Scientific Reports 2013 3:1* 3 (1 Sept. 2013), pp. 1–6. ISSN: 2045-2322. DOI: 10.1038/srep02810.

[13] J. E. Gubernatis and T. Lookman. "Machine learning in materials design and discovery: Examples from the present and suggestions for the future". In: *Physical Review Materials* 2 (12 Dec. 2018). ISSN: 24759953. DOI: 10.1103/PhysRevMaterials.2.120301.

[14] Bohayra Mortazavi et al. "Exploring thermal expansion of carbon-based nanosheets by machine-learning interatomic potentials". In: *Carbon* 186 (Jan. 2022), pp. 501–508. ISSN: 0008-6223. DOI: 10.1016/J.CARBON.2021.10.059.

[15] P. Hohenberg and W. Kohn. "Inhomogeneous Electron Gas". In: *Phys. Rev.* 136 (3B Nov. 1964), B864–B871. DOI: 10.1103/PhysRev.136.B864.

[16] Xavier Gonze et al. "The Abinitproject: Impact, environment and recent developments". In: *Computer Physics Communications* 248 (2020), p. 107042. ISSN: 0010-4655. DOI: https://doi.org/10.1016/j.cpc.2019.107042.

[17] W. Kohn and L. J. Sham. "Self-Consistent Equations Including Exchange and Correlation Effects". In: *Phys. Rev.* 140 (4A Nov. 1965), A1133–A1138. DOI: 10.1103/PhysRev.140.A1133.

[18] Anubhav Jain et al. *Commentary: The materials project: A materials genome approach to accelerating materials innovation*. 2013. DOI: 10.1063/1.4812323.

[19] John P. Perdew, Kieron Burke, and Matthias Ernzerhof. "Generalized Gradient Approximation Made Simple". In: *Phys. Rev. Lett.* 77.18 (Oct. 1996), pp. 3865–3868. ISSN: 0031-9007, 1079-7114. DOI: 10.1103/physrevlett.77.3865.

[20] William G. Hoover. "Canonical dynamics: Equilibrium phase-space distributions". In: *Phys. Rev. A* 31 (3 Mar. 1985), pp. 1695–1697. DOI: 10.1103/PhysRevA.31.1695.

[21] Keivan Esfarjani et al. "On the importance of optical phonons to thermal conductivity in nanostructures". In: *Applied Physics Letters - APPL PHYS LETT* 99 (Aug. 2011). DOI: 10.1063/1.3615709.

[22] Atsushi Togo et al. "Implementation strategies in phonopy and phono3py". In: *J. Phys. Condens. Matter* 35.35 (2023), p. 353001. DOI: 10.1088/1361-648X/acd831.

[23] Atsushi Togo. "First-principles Phonon Calculations with Phonopy and Phono3py". In: *J. Phys. Soc. Jpn.* 92.1 (2023), p. 012001. DOI: 10.7566/JPSJ.92.012001.

[24] Olle Hellman et al. "Temperature dependent effective potential method for accurate free energy calculations of solids". In: *Phys. Rev. B* 87 (10 Mar. 2013), p. 104111. DOI: 10.1103/PhysRevB.87.104111.

[25] Olle Hellman and David A Broido. "Phonon thermal transport in Bi_2Te_3 from first principles". In: (2014). DOI: 10.1103/PhysRevB.90.134309.

[26] O. Hellman, I. A. Abrikosov, and S. I. Simak. "Lattice dynamics of anharmonic solids from first principles". In: *Phys. Rev. B* 84 (18 Nov. 2011), p. 180301. DOI: 10.1103/PhysRevB.84.180301.

[27] Aloïs Castellano. "Étude des effets de la température sur les combustibles nucléaires par une approche ab initio". In: (Jan. 2022).

[28] Albert P. Bartók et al. "Gaussian approximation potentials: The accuracy of quantum mechanics, without the electrons". In: *Physical Review Letters* 104 (13 Apr. 2010). ISSN: 00319007. DOI: 10.1103/PhysRevLett.104.136403.

[29] Ivan S Novikov et al. "The MLIP package: moment tensor potentials with MPI and active learning". In: *Machine Learning: Science and Technology* 2 (2 Dec. 2020), p. 025002. ISSN: 2632-2153. DOI: 10.1088/2632-2153/ABC9FE.

[30] A. P. Thompson et al. "Spectral neighbor analysis method for automated generation of quantum-accurate interatomic potentials". In: *Journal of Computational Physics* 285 (Mar. 2015), pp. 316–330. ISSN: 0021-9991. DOI: 10.1016/J.JCP.2014.12.018.

[31] Jörg Behler. "Perspective: Machine learning potentials for atomistic simulations". In: *Journal of Chemical Physics* 145 (17 Nov. 2016). ISSN: 00219606. DOI: 10.1063/1.4966192.

[32] Yunxing Zuo et al. “Performance and Cost Assessment of Machine Learning Interatomic Potentials”. In: *Journal of Physical Chemistry A* 124 (4 Jan. 2020), pp. 731–745. ISSN: 15205215. DOI: 10.1021/acs.jpca.9b08723.

[33] A. P. Thompson et al. “LAMMPS - a flexible simulation tool for particle-based materials modeling at the atomic, meso, and continuum scales”. In: *Comp. Phys. Comm.* 271 (2022), p. 108171. DOI: 10.1016/j.cpc.2021.108171.

[34] Ask Hjorth Larsen et al. “The atomic simulation environment—a Python library for working with atoms”. In: *Journal of Physics: Condensed Matter* 29.27 (2017), p. 273002.

[35] S. R. Bahn and K. W. Jacobsen. “An object-oriented scripting interface to a legacy electronic structure code”. English. In: *Comput. Sci. Eng.* 4.3 (May 2002), pp. 56–66. ISSN: 1521-9615. DOI: 10.1109/5992.998641.

[36] M.J. van Setten et al. “The PseudoDojo: Training and grading a 85 element optimized norm-conserving pseudopotential table”. In: *Computer Physics Communications* 226 (2018), pp. 39–54. ISSN: 0010-4655. DOI: https://doi.org/10.1016/j.cpc.2018.01.012.

[37] Bahadur Singh et al. “Stable charge density wave phase in a 1T-TiSe2 monolayer”. In: *Physical Review B* 95 (24 June 2017). ISSN: 24699969. DOI: 10.1103/PhysRevB.95.245136.

[38] Sadhu Kolekar et al. “Layer- and substrate-dependent charge density wave criticality in 1T–TiSe2”. In: *2D Materials* 5 (1 Oct. 2017), p. 015006. ISSN: 2053-1583. DOI: 10.1088/2053-1583/AA8E6F.

[39] Axel D. Becke and Erin R. Johnson. “A simple effective potential for exchange”. In: *The Journal of Chemical Physics* 124.22 (2006), p. 221101. DOI: 10.1063/1.2213970.

[40] John P. Perdew and Yue Wang. “Accurate and simple analytic representation of the electron-gas correlation energy”. In: *Phys. Rev. B* 45.23 (June 1992), pp. 13244–13249. ISSN: 0163-1829, 1095-3795. DOI: 10.1103/physrevb.45.13244.

[41] James W. Furness et al. “Accurate and Numerically Efficient r2SCAN Meta-Generalized Gradient Approximation”. In: *The Journal of Physical Chemistry Letters* 11.19 (2020). PMID: 32876454, pp. 8208–8215. DOI: 10.1021/acs.jpclett.0c02405.

[42] James W. Furness et al. “Correction to “Accurate and Numerically Efficient r2SCAN Meta-Generalized Gradient Approximation””. In: *The Journal of Physical Chemistry Letters* 11.21 (2020). PMID: 33073997, pp. 9248–9248. DOI: 10.1021/acs.jpclett.0c03077.

[43] A. M. Ghorayeb and R. H. Friend. "Transport and optical properties of the hydrazine intercalation complexes of TiS2, TiSe2 and ZrS2". In: *Journal of Physics C: Solid State Physics* 20 (26 Sept. 1987), p. 4181. ISSN: 0022-3719. DOI: 10.1088/0022-3719/20/26/019.

[44] R. H. Friend et al. "Semimetallic character of TiSe2 and semiconductor character of TiS2 under pressure". In: *Journal of Physics C: Solid State Physics* 10 (24 Dec. 1977), p. L705. ISSN: 0022-3719. DOI: 10.1088/0022-3719/10/24/006.

[45] Dinh Loc Duong, Marko Burghard, and J. Christian Schön. "Ab initio computation of the transition temperature of the charge density wave transition in TiS e2". In: *Physical Review B - Condensed Matter and Materials Physics* 92 (24 Dec. 2015). ISSN: 1550235X. DOI: 10.1103/PhysRevB.92.245131.